Diffuse Optical Tomography: DOT, NIRS and fNIRS

General Principle

Diffuse optical tomography, or DOT, aims at the resolution of the spatial distribution of optical properties in highly scattering media. Near-Infrared Spectroscopy (NIRS) is a synonym for the same technique. NIRS used for functional imaging of brain activity is usually called Functional Near-Infrared Spectroscopy, fNIRS. Biomedical applications of DOT are based on illumination of thick tissue by NIR light, detection of diffusely transmitted or reflected light, or fluorescence of endogenous or exogenous fluorophores [257, 868, 1228]. Typical applications of DOT techniques are optical mammography, brain imaging, and non-invasive investigations of drug effects in small animals.

Scattering and Absorption in Biological Tissue

Scattering in biological tissue is not isotropic. A considerably larger amount of light is scattered forward rather than in reverse [808, 1228]. For describing the penetration of light into thick tissue it is, however, sufficient to assume isotropic scattering with a reduced scattering coefficient. The reduced scattering coefficient, μ'_s, is

$$\mu'_s = \mu s\,(1 - g)$$

with g being the average cosine of the scattering angle. For biological tissue g is typically in the range from 0.7 to 0.9 [303]. Reduced scattering coefficients for various types of tissue are given in [808].

Typical values of μ'_s are around 10 cm^{-1}. Consequently, there are practically no unscattered or 'ballistic' photons for tissue thicker than 1 cm. Instead, the photons must be considered to diffuse through the tissue. Consequently, the spatial resolution of DOT images is extremely poor and cannot compete with positron emission, X ray and MRI techniques.

The NIR absorption in tissue is dominated by oxy-haemoglobin, deoxy-haemoglobin, lipids, and water [303]. There is an absorption minimum from approximately 650 to 900 nm. Therefore, NIR light can be transmitted and detected through tissue layers as thick as 10 cm. Absorption coefficients for various types of tissue are given in [808].

In spite of the poor spatial resolution, DOT in the NIR has the benefit that the measured absorption coefficients are related to the biochemical constitution of the tissue, such as haemoglobin concentration and blood oxygenation [303, 768]. If exogenous markers are used, the absorption or fluorescence delivers additional information about blood flow, blood leakage, ion concentrations, or protein binding state.

In images obtained by continuous illumination and detection it is difficult to distinguish between the effects of scattering and absorption. The situation is much better if pulsed or modulated light is used to transilluminate the tissue and the pulse shape or the amplitude and phase of the transmitted light are recorded. The general effect of variations in the scattering and absorption on the shape of the transmitted pulses is shown in Fig. 751.

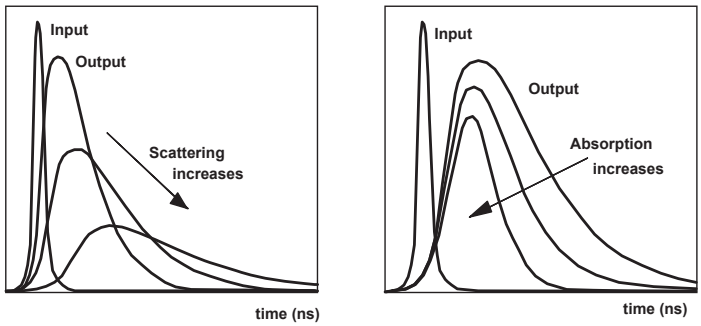

Fig. 751: Effect of scattering and absorption on the shape of a pulse transmitted through thick tissue

Both increased scattering and increased absorption decrease the integral output intensity. However, increased scattering increases the pulse width, while increased absorption decreases it. Therefore, the shape of the 'time-of-flight distribution' of the photons in combination with the intensity can be used to distinguish between changes in scattering and absorption.

Spatial Resolution

DOT is targeting not only at recording scattering and absorption coefficients but also at resolving their spatial distribution. Of course, scattering acts as a spatial low-pass filter, and quickly smoothes out details with increasing depth in the tissue. Reconstruction of the internal tissue structure is normally limited to details no smaller than the depth in which they are located.

The options of reconstructing are improved by using temporal resolution: Photons arriving at early times have travelled a shorter distance in the tissue than later photons. On average, they have taken a more direct path through the tissue. Images built up from early photons therefore yield a noticeably better spatial resolution, see [687, 837, 1167, 1187].

Moreover, in diffuse reflection experiments (i.e. with the source and the detectors at the same side of the tissue) the depth of scattering and absorption changes in the tissue can be derived from time-resolved data much better than from intensity data [513, 1079].

The computation of the spatial distribution of absorption and scattering can be considerably simplified by using the first and second moments, i.e. the mean time of flight and the variance of the time of flight [715, 718]. It has been shown that variations of the absorption and scattering coefficients calculated from the moments are obtained from considerably larger depth than such calculated from the intensity. The situation is shown qualitatively in Fig. 752.

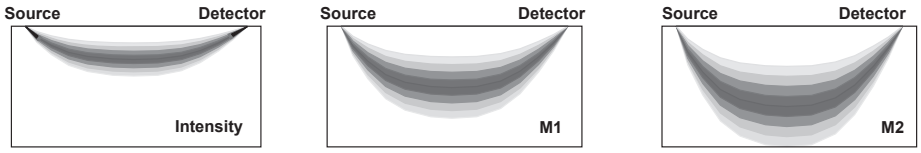

Fig. 752: Diffuse reflection experiment, depth in the tissue from which changes in the absorption and scattering coefficients are obtained. Left calculation from intensity data, middle calculation from M1 (mean time of flight), right calculation from M2 (variance of time of flight)

The banana-shaped pattern shows the depth from which absorption and scattering changes are obtained. Please note that it does *not* represent anything like the mean path of the photons. For a detailed discussion and Monte-Carlo calculations please see Wabnitz et al. [1190].

The complete reconstruction of tissue structures and optical properties from time resolved data is extremely demanding and not entirely solved yet. A number of different approaches are used to solve the 'inverse problem' of DOT [30, 31, 259, 392, 395, 429, 844, 886, 1146, 1187].

Instrumental Approaches

All approaches use a large number of time-resolved detection channels of different wavelengths, source-detector distance, or different location or transillumination angle. The time-channel width required to quantify absorption and reduced scattering coefficient is on the order of 10 ps [844]. Moreover, low-noise data are required to reconstruct the tissue properties from the relatively small intensity and pulse shape changes. This requires to record a large number of photons. Because the illumination intensity and the measurement time for in vivo measurements are limited a high detection efficiency is essential. Detection efficiency becomes even more important if fluorescence is to be detected in combination with normal DOT. Therefore the instruments normally use simultaneous detection in many time-resolved channels. Two typical setups used in DOT are shown in Fig. 753.

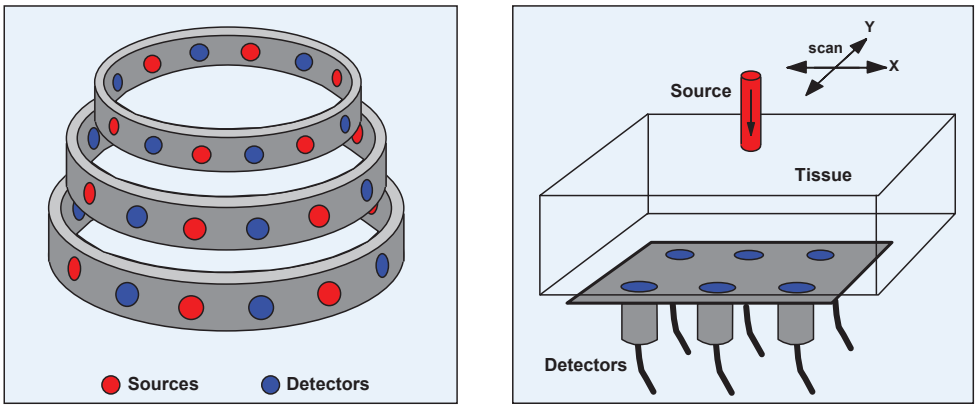

Fig. 753: Source-detector setups for optical tomography. Left: Circular arrangement of sources and detectors. Right: Scanning setup with one source and several detectors. Source and detectors are scanned simultaneously across the sample.

The traditional tomography setup is shown left. A large number of sources and detectors are arranged around the sample. The light sources are switched on one after another. For each source, time-of-flight distributions are recorded by all detectors [32, 433, 514, 842, 980]. The setup is used for breast imaging and infant brain imaging. Because the setup is compact, mechanically simple, and can be built from purely non-metallic materials it is also used for optical tomography in conjunction with MRI imaging [841, 843]. When the setup is used for adult brain imaging, the detectors opposite to the source do not detect reasonable signals. Therefore detectors and sources are arranged at only side of the head. The configuration can be considered a sub-set of the arrangement shown in Fig. 753, left.

The right setup uses a scanning technique. Several lasers of different wavelength are multiplexed into a single optical source. The light source and the detector, or a number of detectors, are scanned simultaneously across the sample. The scanning technique is successfully used for optical mammography [306, 473, 474, 476, 887, 930, 1117, 1118, 1145, 1146]. A scanning setup for small-animal imaging is described in [425]. The benefit of scanning is that it obtains a high spatial density of data points. Therefore the Nyquist condition is fulfilled for both spatial dimensions. However, problems can arise from edge effects. Not only can the detectors be damaged if the scan runs over the edge of the sample, but also the reconstruction of the sample properties has to cope with different photon migration near the edge. The problem can be solved by immersing the sample into a matching fluid [1188].

In both setups different wavelengths are multiplexed into the optical source channels. The wavelengths can be multiplexed on a pulse-by pulse basis and recorded in the same TAC interval or in longer intervals and recorded in different memory blocks by using the multiplexing capability of the SPC modules. The advantage of the second technique is that there is no

crosstalk between the wavelength channels and reduced signal distortion due to pile-up effects. Please see Multiplexing of Lasers, page 287.

On the detection side, frequency domain instruments using modulation techniques are competing with time-domain instruments using gated image intensifiers, and instruments based on TCSPC. An overview on TCSPC-based DOT techniques has been given in [140], an overview on frequency-domain DOT techniques can be found in [249]. It is now commonly believed that TCSPC instruments are more complex, but superior in terms of efficiency and sensitivity. The excellent results obtained with TCSPC-based instruments under clinical conditions clearly confirm the applicability of TCSPC to DOT [476, 477, 719, 930, 906, 1117, 1118].

Many TCSPC-based DOT instruments still use single lasers or several multiplexed lasers and record in a single SPC-330 or SPC-630 channel [301, 474, 475, 476, 477, 715, 888, 930, 1145]. Multi-detector operation of up to eight detectors connected to a single SPC-330 or SPC-630 channel was used in [302, 305, 306, 842, 843, 1147]. A system with 32 fully parallel TCSPC channels based on conventional NIM modules was described in [980] and used for breast and brain imaging [514, 515, 517].

Recent TCSPC-based instruments use the bh SPC-134 or SPC-154 packages of four, in some cases eight parallel TCSPC devices [130, 575, 718, 719, 887, 889, 1117, 1118, 1146, 1174, 1188, 1189]. The number of detector channels is often increased by routers, see for example [286].

Optical tomography techniques for human medicine are currently at the stage of clinical tests. This causes a data compatibility problem between the different instruments. Optical mammographs and brain imagers are complex instruments with their own data acquisition and data processing software. Even if the instruments are based on time-resolved detection by TCSPC they may not use exactly the same procedures and data processing algorithms. To keep the clinical data obtained by different instruments comparable exact protocols for quality assessment have to be defined [890, 1191, 1192].

Scanning Mammography

A recent overview on Time-Resolved Optical Mammography has been given by Quarto et al. [906]. The principle of a typical TCSPC-based scanning mammograph is shown in Fig. 754.

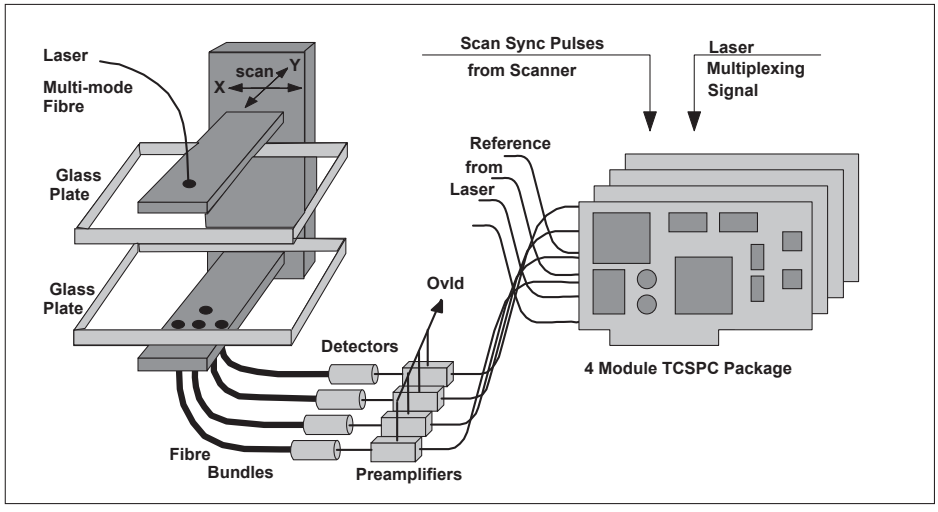

Fig. 754: General principle of a TCSPC scanning mammograph

The breast is slightly compressed between two glass plates. Due to the high sensitivity of TCSPC compression to about 6 cm is sufficient to obtain enough signal at the detectors.

The laser light is delivered via a multi-mode fibre. The transmitted light is collected by four fibre bundles and fed into four detectors. Fibres and fibre bundles are certainly not a favourable solution in terms of pulse dispersion, timing stability and detection efficiency. However, they decouple the electrical part of the system from the patient. The fibres are therefore an important part of the system to satisfy safety regulations for medical instruments.

Both the source fibre and the detection fibre bundles are assembled on a scanning stage. One scan typically contains 1000 to 5000 pixels, enough to avoid artefacts due to spatial undersampling. The scan amplitudes and the shape of the scanning area are different for different patients. To ensure that the detectors are not damaged by overload, the scanner must be prevented from running beyond the edge of the breast. This is achieved by using preamplifiers with overload detection (see ‘Preamplifiers and Detector Control’, page 191). When the detector currents exceed a reasonable limit the scan direction is reversed.

The four detector signals are connected into individual channels of a four-module TCSPC system. In practice, variable neutral-density filters and long-pass filters are placed in front of the detectors to compensate for different intensity at different breast thickness and to reduce the daylight sensitivity.

Usually several laser wavelengths are multiplexed into a single source fibre. Typical wavelengths used in mammography are between 685 and 785 nm. However, in the last few years more and more wavelengths have been added: 635 nm is used to obtain better general absorption contrast [1118]. Wavelengths from 905 nm to 975 nm deliver information about water and lipid contents [1117]. Recently even 1060 nm has been used to detect collagen in the breast tissue [1121, 1122]. An application to the identification of healthy subjects who are at risk to develop breast cancer was described in [1124].

The wavelengths can be multiplexed on a pulse-by pulse basis and recorded in the same TAC interval [476, 887, 930, 1117, 1118, 1145, 1146] or in intervals of 50 to 200 µs (2500 to 10.000 pulses) and recorded in different memory blocks by using the routing capability of the SPC modules (see Fig. 430, page 287). The benefit of the second technique is that there is no crosstalk between the wavelength channels, and signal distortion due to pile-up effects is reduced.

The number of wavelength channels can be increased by generating a super-continuum in a photonic crystal fibre and TCSPC multi-wavelength detection [48, 49, 1070]. The technique delivers superior spectral data. As long as Titanium-Sapphire lasers had to be used to excite the super-continuum the technique was too expensive for routine application. Recently introduced super-continuum sources based on fibre lasers have changed the situation. These light sources can be used in not only in combination with multi-wavelength TCSPC but also with wavelength multiplexing via tuneable acousto-optical filters, see section ‘Tissue Scanning System with Laser Wavelength Multiplexing’ in this chapter.

The recording in the TCSPC channels can be synchronised with the scanning by software. In this case the time-of-flight distributions are read out from the TCSPC modules for each individual pixel. The bh SPC-630 and SPC-130/134 modules can avoid devoting time to readout during the scan by using sequential recording in the Continuous Flow mode (see ‘Sequential Recording’ page 104). Another convenient mode is hardware-controlled scanning (see ‘Tissue Scanning System with Laser Wavelength Multiplexing’, page 569) and synchronisation of the data acquisition via the Frame, line and pixel clock pulses. In this mode the TCSPC modules hold the time-of-flight distributions of all pixels of a scan in their memories. The data are read out when the scan is completed. It must, however, be taken into account that the length of the lines of the scan varies since the return points of the scan are controlled by the detector over-

load signals. Therefore, the scan software must store the positions of the return points and the number of pixels between. These positions are used later to adjust the lines horizontally.

In the last few years it is increasingly attempted to use fluorescence of contrast agents in addition to diffuse reflectance or transmittance. A scanning system that records images of the time-resolved fluorescence, diffuse fluorescence, diffuse transmittance, and fluorescence from both sides of an object was described in [211]. The data in the four channels were recorded by an SPC-134 TCSPC system. The instrument was demonstrated on phantoms containing a fluorescent inclusion but is, in principle, be applicable also to breast imaging.

If fluorescence is to be detected in combination with DOT, detection efficiency may become a crucial point. The detection efficiency increases with the total detection area and, therefore, with the number of detectors. It can therefore be advantageous to use more than the four detectors shown in Fig. 754. In that case, several detectors are connected to one TCSPC channels via a router.

Fig. 755, left, shows the time-of-flight distributions for four detectors detecting at different projection angles at a single pixel of a breast scan. The acquisition time was 100 ms per pixel. The source-detector geometry is shown at right. The time offsets between the curves are due to different delays in the fibre bundles, detectors, and TCSPC channels. Mammograms were calculated from the photons in the 8th of 10 equidistant time windows spread over the time-of-flight distribution. The result [130] is shown in Fig. 756.

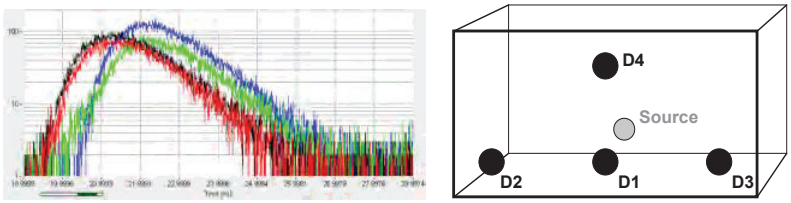

Fig. 755: Left: Time-of-flight distributions in one pixel of a breast scan. Different projection angels, acquisition time 100 ms per pixel. Right: Detector and source configuration. D1 is the direct detector, D2, D3 and D4 are offset by 2 cm.

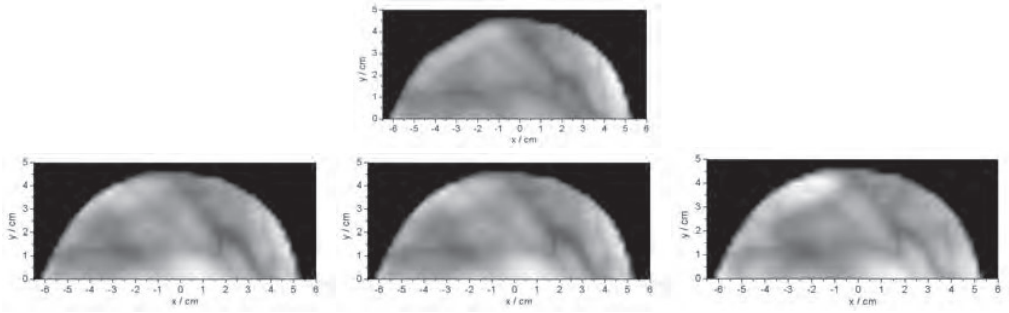

Fig. 756: Mammograms of a healthy volunteer recorded simultaneously at four projection angles. The images were generated from photon counts in a late time window. The arrangement of the mammograms corresponds to that of the detectors D1-D4 in Fig. 755. From [130]

Images in early and late time windows show qualitatively the scattering and the absorption in the tissue [300]. They can therefore be used to distinguish tumours in breast tissue. Most tumours have increased absorption due to increased haemoglobin content and blood leakage. These tumours are therefore prominent in the late time window. Cysts have decreased scattering and are visible in early time windows [1117]. An additional benefit of the late time window is that the images are almost free of edge effects [474].

Breast imaging has also been performed in a two-dimensional modification of the classic tomography setup. A technical system based on an SPC-134 and fibre switches for the source

and detector position has been described by Gao et al. [1269], reconstruction algorithms was by Yang et al. [1245], a pilot study has been presented by Zhang et al. [433].

When quantitative data of the absorption and reduced scattering coefficients are needed this requires the application of an appropriate analytical model [259, 258, 1187]. The modelled distribution is convoluted with the IRF and fitted to the measured time-of-flight distributions in the individual pixels at several wavelengths [474, 476, 1069, 1146]. A comparison of the accuracy of scattering and absorption coefficients obtained by a time-window technique and by fitting a homogeneous diffusion model to the data is given in [300]. In-vivo applications and results of clinical studies were presented in [476, 477, 478, 479, 480, 488, 896, 906, 929, 930, 1117, 1119, 1123, 1124].

Static Brain Imaging

Structural tomography data of the brain are acquired in the traditional tomography setup, see Fig. 753, left. For each source position time-of-flight distributions are recorded for all laser wavelengths in all detector channels. Switching between the source positions is performed by fibre switches. The time-of-flight distributions at the detector positions can be recorded sequentially by another fibre switch as described by Gao et al. and Lu et al. [433, 733]. An improved architecture that uses the four parallel TCSPC channels of an SPC-134 and multiplexes four signals into the detector of each channel by 4:1 fibre switches has been described in [432]. Both instruments have been used for phantoms but are basically capable of recording static brain images. Fibre switching is a cost-efficient way to record at many source and detector positions. However, it makes the measurement slow and inefficient in terms of photon efficiency. The measurement can be made faster and the efficiency be increased by recording the time-of-fight distributions all detector positions in parallel. For static brain imaging this is usually performed by several TCSPC modules and routers, as shown in Fig. 757.

A recent instrument of this type has been described by Cooper et al. [291]. Named ‘MONSTIR II’, the instrument has 4 SPC-150 TCSPC modules, four HRT-81 routers, and 32 detectors. 4 wavelengths of an SC450 Fianium supercontinuum laser are multiplexed via AOTFs. All in all, 128 signals for different combinations of laser wavelength and detector position are recorded for every source position.

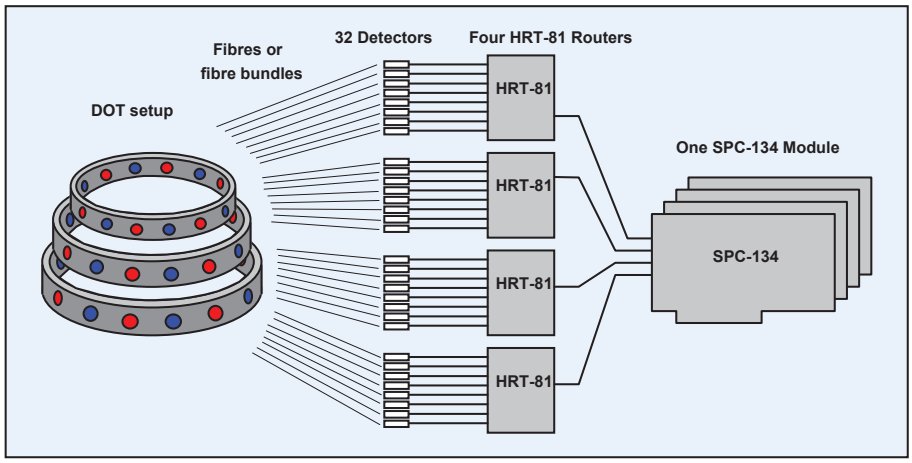

Fig. 757: Connecting a 32-channel tomography setup to an SPC-134 for-channel TCSPC package

In systems like the one shown above the count rates in the individual detector channels may differ over a wide range depending on the distance from the source. For channels directly adjacent to the current source position, the count rate can be as high as several MHz. The PMTs

can even be driven into overload. On the other hand, channels opposite to the source position may not collect any reasonable number of photons at all. In a TCSPC system with routers, the overloaded detector may block the router to which it is connected and thus prevent other signals from being recorded. Therefore, if the count rate of a detector becomes too high, either this detector must be switched off or an automatic intensity regulator of some kind must be placed in front of the detectors.

Typical time-of-flight distributions are shown in Fig. 758. The curves were recorded with a bh BHLP-700 diode laser of 2.5 mW power, 785 nm wavelength, and 50 MHz repetition rate. The detector was a bh PMC-100-20. The curves show the time-of-flight distribution for two different locations at the forehead together with the instrument response function. The source-detector distance was 6 cm. The acquisition time was 20 s, the count rates were between 800 kHz and 1 MHz.

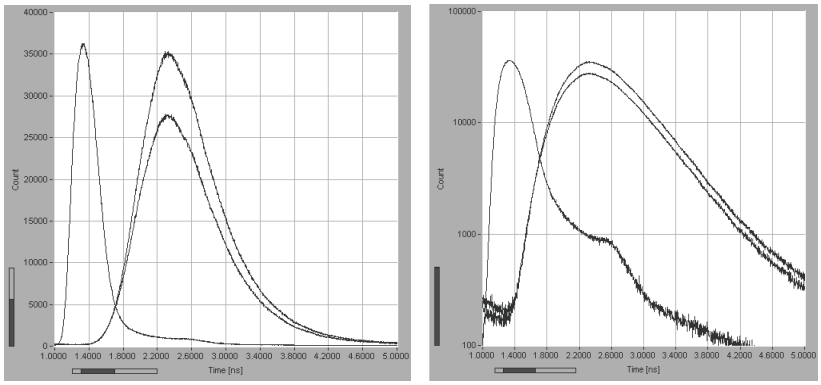

Fig. 758: Time-of-flight curves for two different source and detector positions at the forehead, and instrument response functions. Left linear scale, right logarithmic scale. Source-detector distance 6 cm, Laser 2.5 mW, 785 nm, 50 MHz. Acquisition time 20 s, ADC resolution 4096 channels.

The obtained count rates drop dramatically with increasing source-detector distance. With a laser power of a few mW, meaningful signals can be recorded diametrically through an infant head. For an adult head this is impossible. However, weak signals can be detected from temple to temple, as shown in Fig. 759. With a BHLP-700, 2.5 mW, 785 nm laser and a PMC-100-20 detector a total number of photons of 29,000 and 107,000 was acquired within an acquisition time of 60 s.

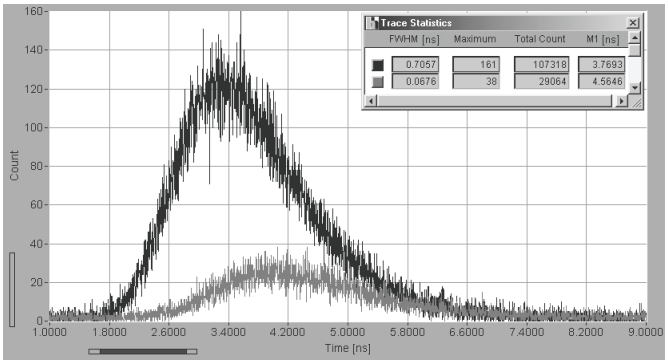

Fig. 759: Time-of flight curves detected from temple to temple through an adult head. Slightly different source and detector positions. Laser power 2.5 mW, wavelength 785 nm, PMC-100-20 detector, acquisition time 60 s, ADC resolution 4096 channels.

Functional Brain Imaging

Dynamic changes in the time-of-flight distributions are caused by the heart beat, variable oxy- and deoxyhemoglobin concentration induced by brain activity, and effects of associated physiological regulation. The haemodynamic response to brain stimulation is on the time scale of a few seconds [370, 411, 412, 1143, 1144].

Recently Liebert et al. have demonstrated that advanced TCSPC is able to record effects of brain activity with 50 ms time resolution, clear separation of scattering and absorption, and better depth resolution than CW or frequency-domain techniques. In particular, moment analysis and time-window analysis of TCSPC data provide a way to distinguish between perfusion changes in the brain and the scalp [290, 562, 714, 717, 718]. Please see [688, 719, 810, 811, 905, 913, 962, 1081, 1082] for technical details, applications, and clinical results. An overview has been given in [722], a comprehensive review can be found in [1150].

Time-domain functional brain imaging instruments normally use bh SPC-154 or SPC-134 four-channel TCSPC systems with four individual detectors and several multiplexed laser diode lasers. A fast sequence of time-of-flight distributions was recorded in consecutive time intervals of 50 to 100 ms. More results obtained with similar instruments are described in [740, 1080, 1191].

Quaresima et al. used a single SPC-630 channel and a multi-anode PMT to record sequences of time-of-flight curves in eight parallel channels [905]. The acquisition time per step of the sequence was 166 ms. The data of five steps were averaged. Values of μ_s' and μ_a were calculated from the averaged data by using a standard model of diffusion theory. An improved instrument of this type used an SPC-134 package with HRT-41 four-channel routers connected to each TCSPC channel [289, 290]. Thus, simultaneous detection in 16 detector channels was achieved. Two lasers were multiplexed by pulse interleaving; 16 source positions were multiplexed by fibre switches. Applications to functional brain imaging are described in [231, 810, 1149].

An instrument with 8 fully parallel TCSPC channels has been described in [575]. The setup uses two SPC-134 packages in one industrial computer. The optical architecture is shown in Fig. 760.

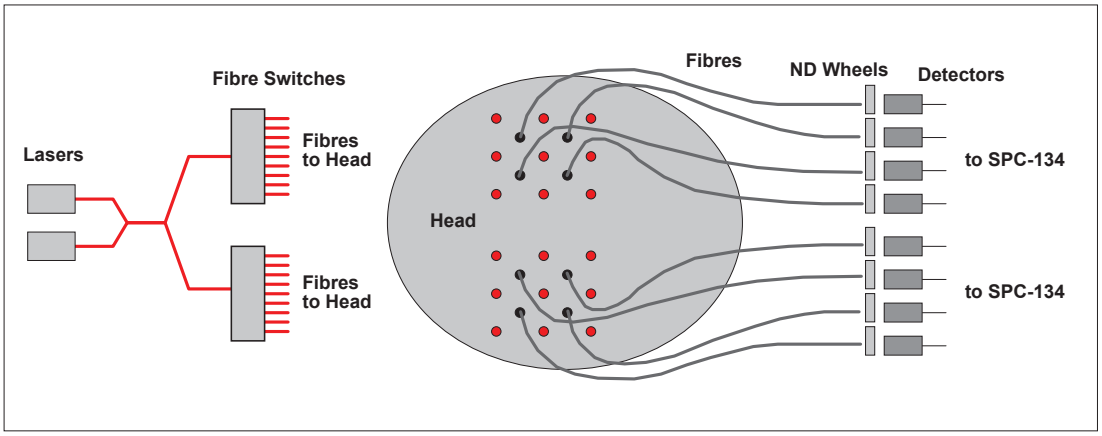

Fig. 760: Optical architecture of the 8-channel parallel DOT system described in [575]

The DTOFS at both sides of the head are recorded simultaneously. For every source position the DTOFs are acquired for 95 ms. One switching cycle through all 9 source positions is completed within 0.9 seconds. Variations of the optical properties in the brain are derived from the intensity and the first and second moments of the time-of-flight distributions [715].

An instrument that multiplexes also the lasers by fibre switches has been described by Re et al. [912]. The system avoids crosstalk of different laser wavelengths by reflections, pile-up, counting loss or detector afterpulsing, see page 287. An application to hemodynamics of the human brain is described by Aletti et al. [11]. The authors show how signal components caused by skin vasomotion and by cerebral perfusion can be separated.

Fig. 761 shows how dynamic DOT data look like. Time-of flight curves of photons transmitted through a forehead were recorded in the continuous flow mode of an SPC-134 system. 20 subsequent time-of-flight curves from the continuous-flow sequence are shown in Fig. 761. The acquisition time was 100 ms per curve, the ADC resolution 1024 channels. The left sequence was detected at a source-detector distance of 5 cm, the right sequence at a distance of 8 cm. The count rates were $1.8 \cdot 10^5$ s^{-1} and $4.5 \cdot 10^6$ s^{-1}, respectively.

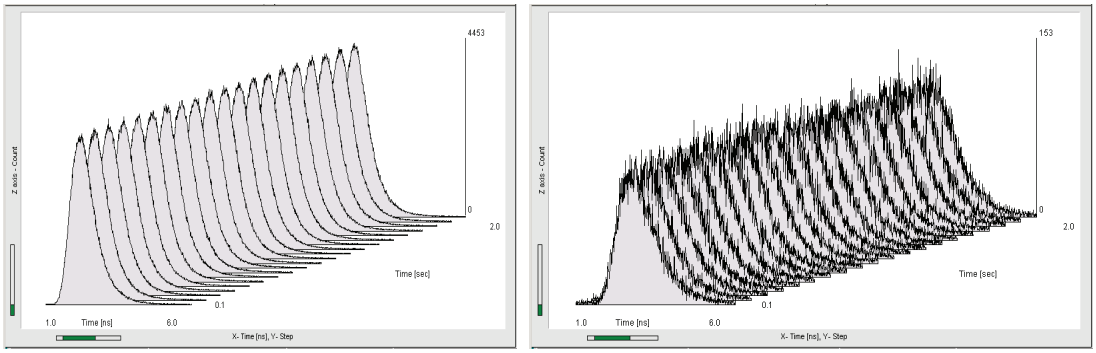

Fig. 761: 20 steps of a TOF sequence recorded in the Continuous Flow mode of an SPC-134. Acquisition time 100 ms per curve, ADC resolution 1024 channels. Left: Source-detector distance 5 cm, count rate $4.5 \cdot 10^6$ s^{-1}. Right: source-detector distance 8 cm count rate $1.8 \cdot 10^5$ s^{-1}

It should be noted that a count rate of $4.5 \cdot 10^6$ s^{-1} is at the very limit of currently available TCSPC devices. Intensity measurements at rates this high require a correction for counting loss (see 'Counting Loss', page 281). The first and second moments of the time-of-flight distributions are not noticeably influenced by counting loss. This is another benefit of the moments technique developed by Liebert et. al.

The standard deviation of the photon numbers and the first moments of the data in Fig. 761, left, is about 0.15 % and 800 fs, respectively. These values are substantially lower than the typical changes caused by the haemodynamic response. In principle, useful response curves could therefore be obtained by recording only a moderate number of stimulation events. However, in practice there is a strong variation in the data due to heart beat and respiration. The haemodynamic brain response can only be separated from these effects by recording a TOF sequence over a large number of stimulation events. Therefore, all the experiments mentioned above used the 'continuous flow' mode of the SPC-134 or SPC-630.

Typical results of haemodynamic response measurements performed by Liebert et al. [714, 718] are shown in Fig. 762. Visual stimulation was used. An annular black and white checkerboard alternating at 8Hz on a computer screen was shown to the patient. During the rest period a dark grey screen was presented while fixation was maintained. The stimulation periods lasting 30s were repeated 20 times separated by 30s of rest. Signals from 20 stimulation periods were averaged. Three multiplexed laser wavelengths were used. The photons were detected by four R7400 PMTs at different source-detector positions. The TOF curves were recorded by an SPC-134 system in the continuous-flow mode. Fig. 762, left to right, shows the intensity change, the change in the mean time of flight, and the change in the variance of the time of flight over the stimulation period. Depth-resolved intra- and extra-cerebral changes of the oxy- and deoxyhemoglobin concentrations calculated from the data of the four detectors at the three wavelengths are shown in Fig. 763.

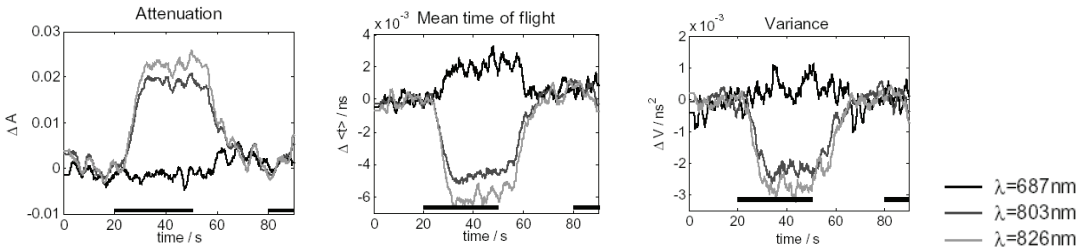

Fig. 762, Left to right: Intensity change, change in the mean time of flight, and change in the variance of the time of flight over the stimulation period. The horizontal bars indicate the periods of stimulation. From Liebert et. al., Proc. SPIE 5138. [714].

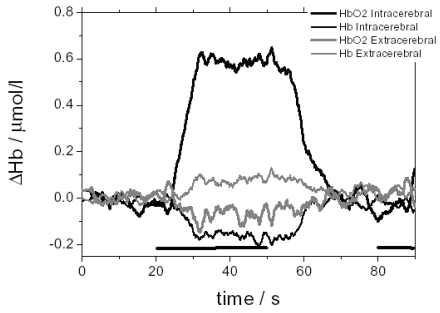

Fig. 763: Intra- and extra-cerebral changes of oxy- and deoxyhemoglobin concentrations during visual stimulation obtained from DTOFs measured at 3 wavelengths and four source-detector separations. The horizontal bars indicate the stimulation period. From [714], Liebert et. al., Proc. SPIE 5138.

Mackert et al. and Sander et al. combined time-resolved reflectance measurement with magneto-encephalography [740, 962]. They used the setup described in [718]. This way, the vascular response could exactly be correlated with the neuronal response.

Perfusion Measurements by ICG Boli

Exogenous absorbers can be used by detecting either their absorption or their fluorescence. The only NIR dye currently approved for use at human patients is indocyanine green (ICG) [328, 812]. Absorption spectra of ICG in water are shown in Fig. 764, left.

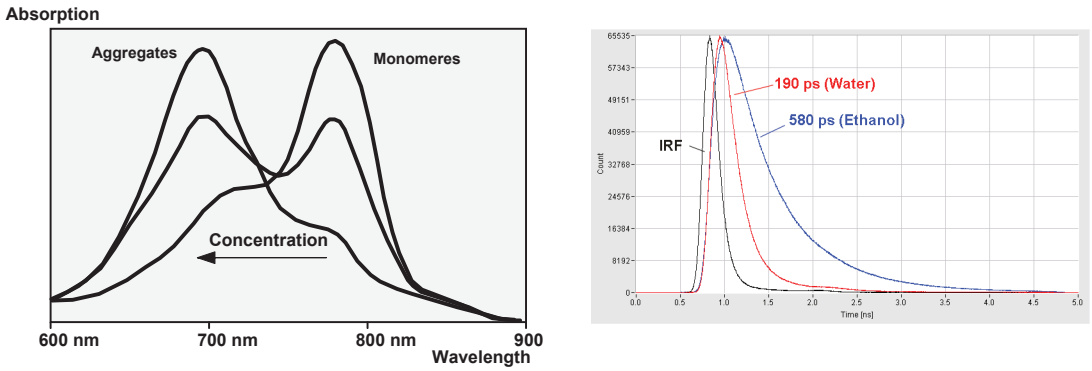

Fig. 764: Left: Absorption spectra for ICG in water, after [328]. Right: Fluorescence decay of ICG in water and ethanol, BHL-600-650 laser, PMC-100-20 detector and SPC-630 TCSPC module.

ICG absorbs strongly between 650 and 820 nm. The absorption of ICG monomers peaks at about 780 nm. In water ICG tends to form aggregates which cause a second absorption band around 700nm. In blood ICG binds to the serum albumin. Aggregation is then largely sup-

pressed, and the absorption around 780 nm dominates. Due to the binding to albumin ICG stays in the blood. It is therefore used as a contrast agent to mark blood vessels.

Fluorescence decay curves of ICG are shown in Fig. 764, right. The fluorescence lifetime in Ethanol is about 580 ps. In water the lifetime is about 190 ps. In both cases the decay functions are multi-exponential, probably due to the presence of monomeric and aggregated forms. The short lifetimes indicate that the fluorescence quantum efficiency is low. Values given in the literature are around 4% [328].

Absorption

In brain imaging ICG can be used to detect blood-flow dynamics. Liebert et al. used the technique for bed-side assessment of cerebral perfusion in stroke patients [719]. A bolus of ICG was injected and the subsequent absorption changes in the tissue monitored. The instrument was essentially the same as used for motor-stimulation experiments [714, 718] (results see Fig. 763). Two multiplexed lasers and four detectors connected to the four TCSPC channels of an SPC-134 package were used. By using the Continuous Flow Mode of the SPC-134, time-of-flight distributions were recorded at a rate of 50 ms per curve. From the time-of-flight distributions the changes in the attenuation, in the mean time of flight, and in the variance of the time of flight were calculated. Fig. 765 shows results for two healthy volunteers, subject 1 and subject 2, and two stroke patients, patient 1 and patient 2 [719]. The curves are sliding averages over 20 subsequent 50-ms recordings. The moments were scaled to a range from 0 to 1 by subtracting the minimum value and normalising the result to its maximum value.

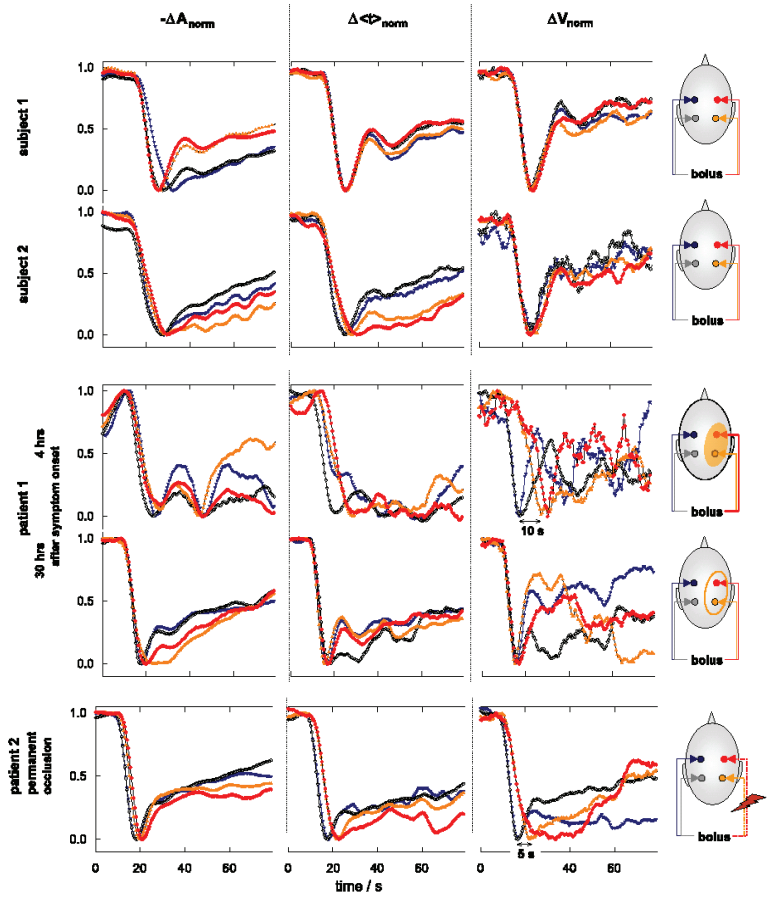

Fig. 765: Changes of the normalised attenuation, $-\Delta A_{norm}$, the mean time of flight, $\Delta\langle t\rangle_{norm}$, and the variance of the time of flight, ΔV_{norm} for two healthy subjects and two stroke patients. The curves were scaled to a range from 0 to 1 by subtracting the minimum value and normalising the result to its maximum. From [719].

For the healthy subjects the changes in the moments appear virtually simultaneously in both brain hemispheres. For the stroke patients the changes in the moments at the location of the stroke are delayed. The delay is most pronounced in the variance, ΔV_{norm}. A thrombolytic therapy of patient 1 resulted in normal perfusion after 30 hours. Patient two had a permanent occlusion.

Absorption changes are not only caused by inflow dynamics of the ICG bolus but also by physiological effects like heart beat, breathing, and blood pressure variations. These effects can be seen as quasi-periodic oscillations in Fig. 765. The mechanisms of these effects and their impact on NIR tissue spectroscopy are discussed in [608].

Diop et al. [345, 346] used the ICG bolus technique to determine cerebral blood flow in piglets under normocapnia, hypercapnia, and carotid occlusion. They compared time-resolved (TCSPC) and CW data recorded under similar conditions. Although the general correlation of the TR and CW data was good the authors also found systematic differences. After discussing possible instrumental effects the authors conclude that the techniques deliver information from different depth in the brain. This is supported by the fact that in the time-resolved data the amplitude of the attenuation change during the bolus is larger for late-arriving photons.

Recently, Liebert et al. described an instrument that records ICG concentration changes at extremely large source-detector distance [721]. By using high incident power from a Ti:Sa laser, and placing a detector directly at the surface of the tissue they were able to record at 9 cm source-detector distance. The instrument was used both on phantoms and on human volunteers. The phantom consists of a fish tank filled with a mixture of milk, water and an absorber. The tank contained a transparent flow-tube through which the same mixture was pumped. In ICG bolus was simulated by injecting ICG in the flow system. The authors showed that the ICG bolus was detectable down to a depth of 5 cm. Measurements at the human head confirmed this result in that they showed physiological effects expected in deep brain layers.

Fluorescence

For a given number of recorded photons, a fluorescence measurement in general yields a better intrinsic SNR than an absorption measurement. The reason is that the dye concentration obtained via fluorescence is directly related to the number of detected photons, whereas the concentration derived from absorption or diffuse reflection is the difference of two photon numbers. However, compared to the diffusely transmitted or reflected intensity the fluorescence intensity is much lower. The SNR actually obtained depends on the efficiency of the optics and the detection system, the tissue thickness, the fluorophore concentration and quantum yield, and the acceptable acquisition time. Milej et al. compared fluorescence and diffuse reflection measurements in phantom experiments. They used a phantom that had tubes for dynamic inflow of indocyanine green (ICG) inserted at different depths. They showed that the use of fluorescence signals delivered better sensitivity and signal-to-noise ratio compared to the use of diffuse reflectance data. A similar study for a fluorescent inclusion within non-fluorescent and weakly fluorescent phantoms came to the same result [576].

Liebert et al. and Milej et al. have shown that the fluorescence of ICG can well be detected from inside the human brain [720, 796, 797]. They used two or four channels of an SPC-134 package. One channel detected the diffusely reflected light, the other the fluorescence. Measurements were performed at a rate of 10 s^{-1}. A result is shown in Fig. 766.

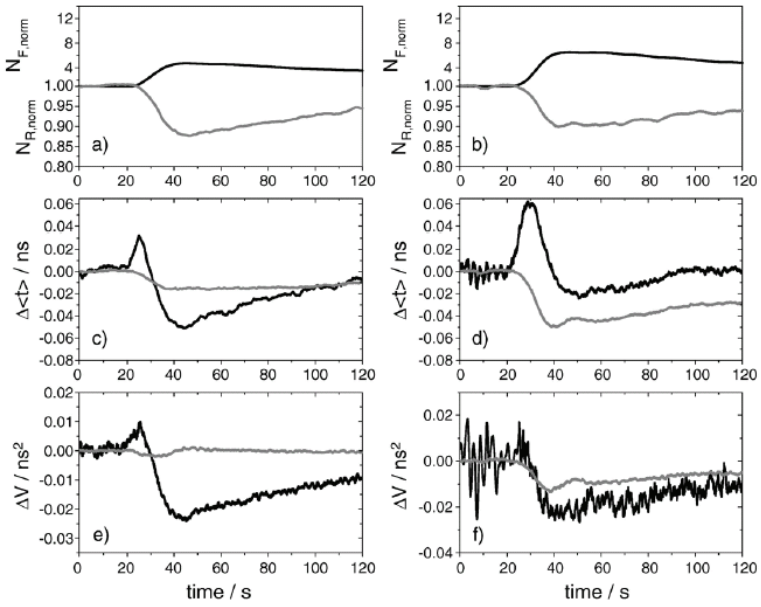

Fig. 766: Normalised number of photons, N_{Rnorm} and N_{Fnorm}, changes in mean time of flight, $\Delta\langle t\rangle$, and changes in variance of time of flight, ΔV, after injection of an ICG bolus. Both hemispheres of brain. Gray curve: Diffuse reflection. Black curve: Fluorescence. From [720], copyright Elsevier Ltd.

The shapes of the curves of the mean time of flight and the variance are significantly different for the fluorescence and the diffuse reflectance. The authors attribute these differences to the time differences of the inflow of the ICG in the intra- and extra-cerebral compartments.

Intra- and extra-cerebral fluorescence components during an ICG bolus have been investigated in detail by Jelzow et al. [561]. The authors present an algorithm to separate these components based on the bolus function and on changes in the DTOFs over the bolus time.

Gerega et al. [445] have demonstrated multi-wavelength fluorescence detection of ICG boli. The authors used a PML-SPEC (MW FLIM) 16-channel detector connected to an SPC-830 TCSPC module. The light from the tissue was collected by a fibre bundle and transferred into the input slit of the PML-SPEC polychromator, see Fig. 767, left. A time-series of multi-wavelength recordings was performed in the Scan Sync Out mode of the SPC-830 module. A result is shown in Fig. 767, right. The authors discuss the effects of absorption, re-absorption, ICG concentration, and depth in the tissue on the recorded data. Please see also a general investigation and discussion of the spectral and temporal fluorescence behaviour of ICG in simulated physiological environment by the same authors [444].

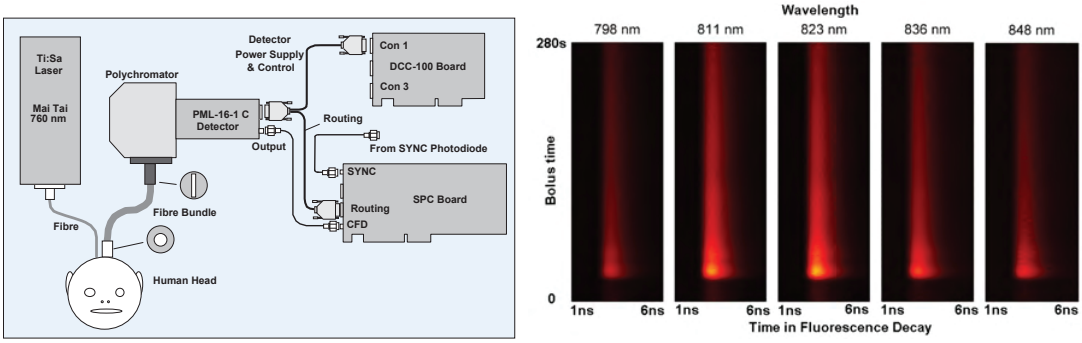

Fig. 767: Setup for time- and wavelength-resolved bolus detection used by [445]

Perfusion Measurement by Diffuse Optical Correlation (DCS)

Perfusion measurements in tissue are also possible by correlating intensity fluctuations of photons scattered in the tissue [261, 347, 1255, 1277]. A laser injects light into the tissue via a fibre. The light at a different spot is collected by another fibre and detected by a photon counting detector. An autocorrelation function of the intensity is calculated from the absolute times of the photons. To obtain a useful correlation function it is required that the laser have a coherence length longer than the average path length in the tissue, and that the fibres have diameters on the order of 20 µm or less. For a test of the principle we used the setup shown in Fig. 768.

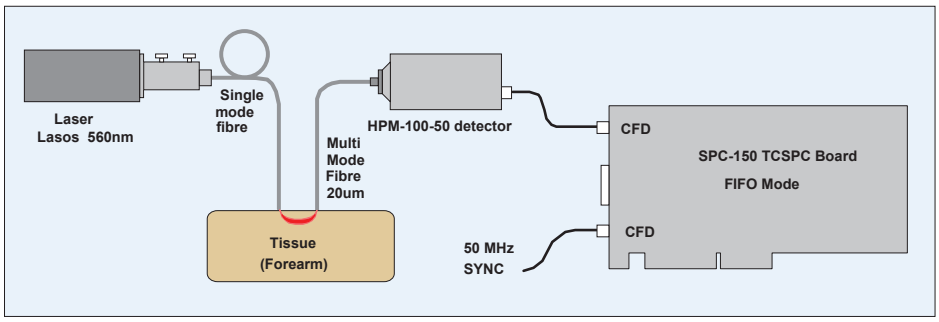

Fig. 768: Test setup for diffuse correlation

Long-coherence length light was delivered by a LASOS DPSS series 561 nm laser. It was injected into the tissue by a single-mode fibre. Diffusely scattered light was collected by a 20 µm multi-mode fibre and detected by an HPM-100-50 hybrid detector. The photons were recorded by an SPC-150 card in the FIFO mode. An autocorrelation function was calculated by the online correlation function of the SPCM software (see page 586). A result is shown in Fig. 769. Because of the unfavourable laser wavelength (we had no long-coherence length laser of longer wavelength) we obtained a count rate of only 25 kHz at a source-detector distance of 3 mm. Nevertheless, there is a clear correlation in the data. The result shows that diffuse correlation can, in principle, be recorded by equipment typically used in TCSPC time-domain DOT.

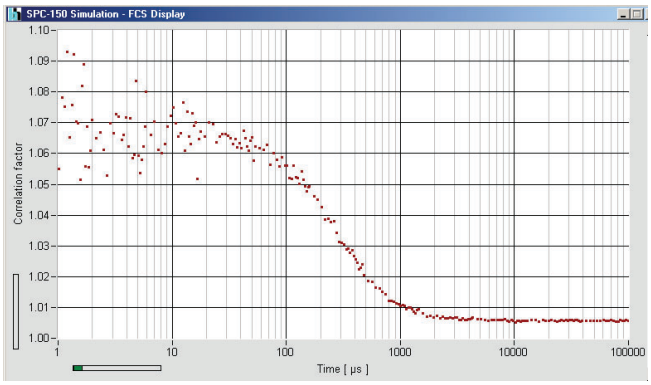

Fig. 769: Correlation curve obtained in the setup shown above. Human forearm, source-detector distance 3 mm, detected count rate 25 kHz.

The setup can easily be extended to 8 detection channels by using a router in front of the SPC-150 card. Correlation can also be obtained by a bh DPC-230 correlator card as has been shown by Diop et al. [347]. In that case, autocorrelation in up to 16 channels can be obtained. An instrument composed of an SPC-134 TCSPC system and a DPC-230 card was used to

combine time-resolved NIRS and DCS for quantification of the cerebral metabolic rate of oxygen consumption [1174].

DOT Experiments at Small Source-Detector Distance

An important parameter of a DOT system of the diffuse reflection type is the maximum depth at which tissue parameters or dynamic variations can be detected. The practical limitation is the rapidly increasing extinction of the optical signal with the path length in the tissue. Theoretically, the path length for a given depth can be reduced by reducing the source-detector distance. Unfortunately, reducing the source-detector system creates another problem: Most of the photons return to the detector after having travelled only a short way through the tissue. The signal intensity in the first few 100 ps after the laser pulse becomes extremely high. The intensity of the later part of the signal, i.e. of the part that has travelled through deep tissue layers, is many orders of magnitude lower. Detecting these photons by the normal time-resolved techniques is impossible: Even if the detector and the TCSPC system could deal with the enormous intensity ratio the photons would be lost in the tail of the IRF and in the afterpulsing of the detector.

It is therefore attempted to suppress the first part of the signal by gating the detector. Fast gating can be obtained in single-photon avalanche diodes (SPADs). However, the on-off ratio of the gating must be on the order of 10^5. Also, the detector must deliver a clean photon timing only a few 100 ps after the 'gate-on' transition. In particular, no electron-hole pairs from the 'gate-off' period must be trapped in the detector and cause avalanche breakdown in the 'gate-on' period. Unfortunately, a lot of such carriers exist in the 'diffusion tail' of a SPAD. Gated detection for zero-distance measurement therefore required substantial improvements in the SPADs and in the quenching and gating circuitry. Other problems are caused by reflections and scattering in the optical system. Also scattered and reflected photons can arrive after the gate-off period and interfere with the 'late photons' returning from deep sample layers. Improvements in SPAD design, theoretical considerations and results of zero-distance DOT can be found are described in [310, 670, 764, 892, 1068, 1071, 1148, 1151]. Please see also 'Gated SPADs, page 180'

Fibre-Based DOT Endoscopes

Laidevant et al. have designed a fibre-based tissue probe arranged around the ultrasound transducer of an endoscopic ultrasound probe [671]. The principle is shown in Fig. 770.

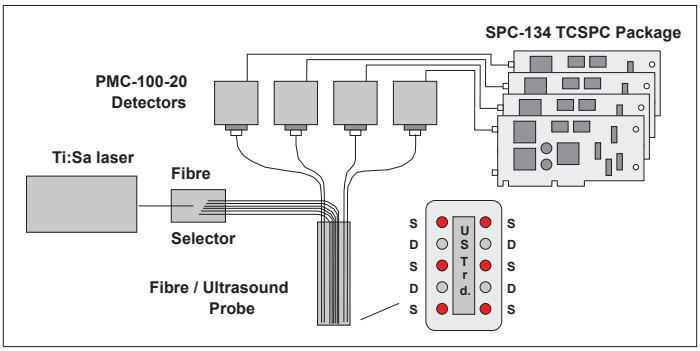

Fig. 770: Fibre based tissue probe with time-resolved detection

6 source fibres and 4 detector fibres are arranged around the ultrasound transducer of the endoscope. The laser is switched periodically through the 6 source fibres. The signals returned through the detector fibres are detected by four PMC-100-20 detectors, and recorded by the four TCSPC modules of an SPC-134 package. The system was tested for fluorescence detec-

tion. By using the temporal data of the four detection channels for the 6 laser positions spatially resolved detection a small ICG inclusion in a scattering medium could be localised at good precision. The optical information is then used to complement the information from the ultrasound transducer.

Tissue Spectrometers

Application of diffuse optical tomography to clinical problems requires that the general optical parameters of different tissue types and their dependence on the wavelength be known. These parameters are determined by recording time-of-flight curves for different source-detector distances at different wavelengths and fitting diffusion models to the results. Because there is no need to resolve fast physiological effects measurements at different source-detector distances and different wavelength are usually performed sequentially. The principle is shown in Fig. 771.

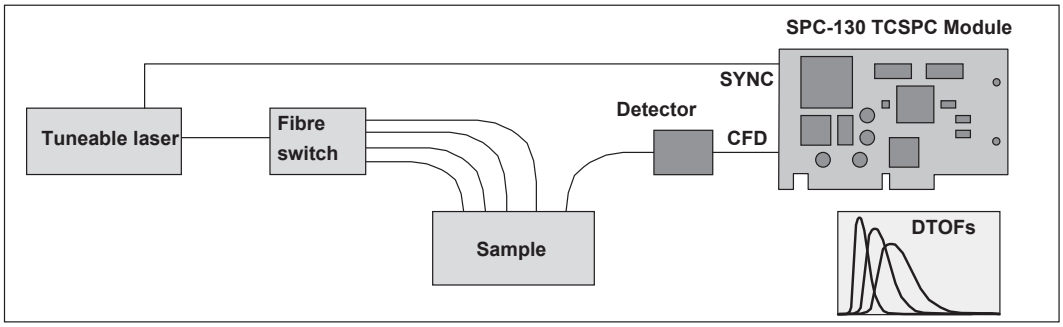

Fig. 771: Principle of a tissue spectrometer with a tuneable laser

A tuneable laser provides light of selectable wavelength. Tissue spectrometers of this type use titanium-sapphire lasers, supercontinuum radiation generated by titanium-sapphire lasers in photonic crystal fibres, supercontinuum lasers with tuneable filters, or tuneable dye lasers pumped by Nd:YLF lasers.

As second way of obtaining spectral information is to illuminate the sample with supercontinuum radiation directly and detect the DTOFs by multi-wavelength TCSPC [48, 313, 457], see Fig. 772.

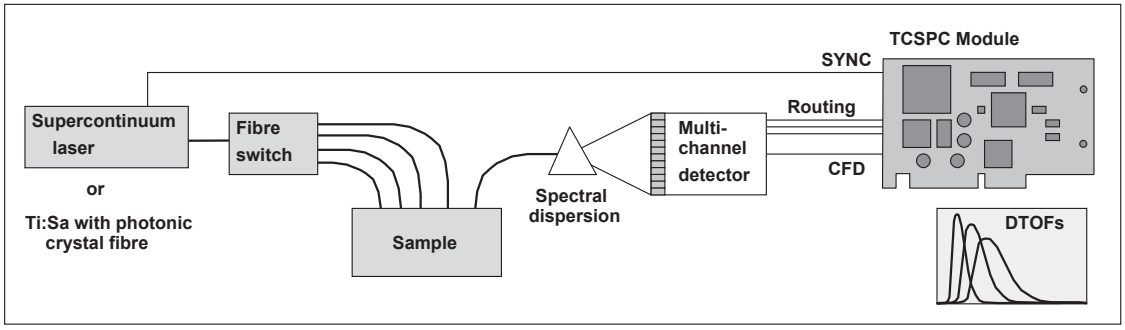

Fig. 772: Principle of a tissue spectrometer with wideband illumination and spectrally resolved detection

Instruments and applications are described in [48, 50, 282, 313, 457, 889, 891, 1120, 1121, 1122, 1107, 1108, 1122]. Gerega et al. used a multi-wavelength detection setup to determine the fluorescence dynamics of ICG in under simulated physiological conditions [442], and discuss the influence of absorption, re-absorption, scattering, and aggregation on the decay profiles at different excitation and emission wavelength. Tissue spectrometers have also been

used in non-medical applications, such as to determine the moisture content of wood, or the quality of food [312, 314, 835, 1141, 1282].

Fibre-Based System for Brain Activation Measurement in Mice

Cui et al. used a fibre-based excitation and detection system to record brain activation in mice during complex tasks [307, 308]. The mice were kept in a compartment which had a food magazine and a lever on each side of the magazine to open it. To open the magazine, the mice had to touch either the left or the right lever. The animals expressed a genetically encoded Ca^{2+} indicator in the brain. The fluorescence of the Ca^{2+} indicator was excited and detected via fibres implanted in the brain. The principle of the fibre-based excitation and detection system is shown in Fig. 773.

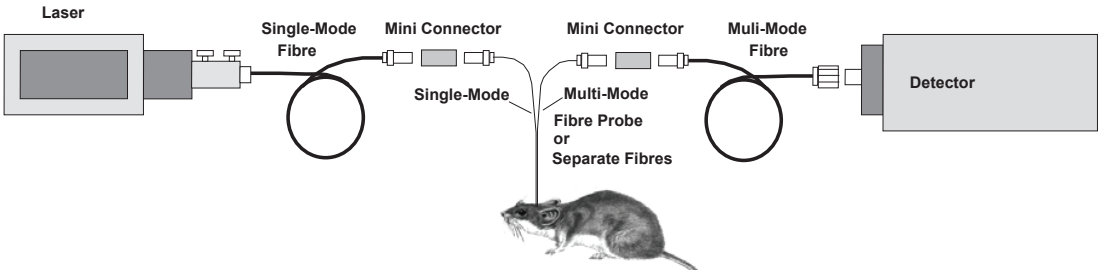

Fig. 773: Principle of fibre excitation and detection system

The excitation light must be transmitted into the brain by a single-mode fibre. A multi mode fibre would generate a speckle pattern the structure of which changes with bending of the fibres and thus induce motion artefacts. The detection fibres are multi-mode to increase the light-collection efficiency. Intensity changes by mode fluctuations do not occur on the detection side because the fluorescence signal is diffusely coupled and has a wide optical spectrum. Excitation and detection fibres (provided by bh) are shown in Fig. 774. The excitation and detection fibres are either separate (Fig. 774, left), or the fibres are mounted in a single excitation/detection probe (Fig. 774, right).

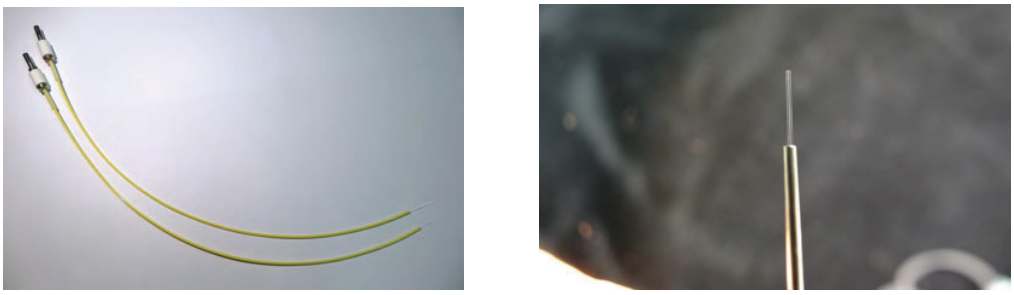

Fig. 774: Excitation and detection fibre (left), combined excitation/detection fibres (right)

For in-vivo applications it is important that the excitation and detection system can be connected and disconnected from the animal. This is achieved by small-size light-weight fibre connectors, Fig. 774, left, upper left. Details of the connectors are shown in Fig. 775. The total weight of the fibre connection is less than 2 g.

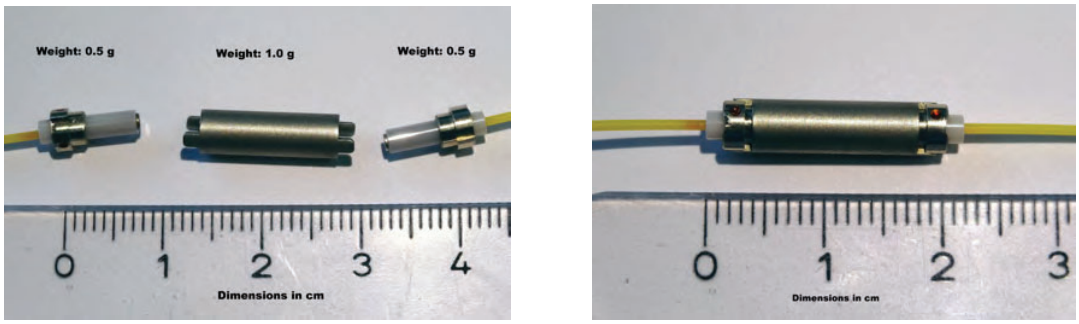

Fig. 775: Fibre mini connectors for excitation and detection fibres. Unconnected (left) and connected (right)

The system was used to detect concurrent activation of the strial direct and indirect pathway during motor activation. The authors were able to record clear differences in the Ca^{2+} signal when the mouse operated either the left or the right lever. Amazingly, the signal was observed about 100 ms before the mouse started to move. That means it was related to the decision to use one or the other lever. Details are described in [307, 308].

Recently, bh have developed a fibre probe with a removable tip, see Fig. 776. the laser is delivered via a single-mode fibre, the fluorescence is detected through a multi-mode fibre. In the tip, both are combined into a short piece of multi-mode fibre. The advantage of this design is that, when the animal is de-coupled from the experiment only the tip remains in it. The disadvantage is possible fluorescence from the tip itself, and from contamination at the interface of the fibres with the tip. Both are transilluminated by the laser, and fluorescence excited in at the interface or in the tip is transferred to the detector. This is no problem for experiment with exogenous fluorophores. For autofluorescence it is, however, critical. By using special glass for the tip, the fluorescence has been kept at a level two orders of magnitude lower than autofluorescence of mammalian tissue. The interface between the fibres and the tip has to be kept absolutely clean. A speck of dust, a single pollen grain, or a fingerprint of the surfaces can make autofluorescence detection impossible. A application has been described in [734].

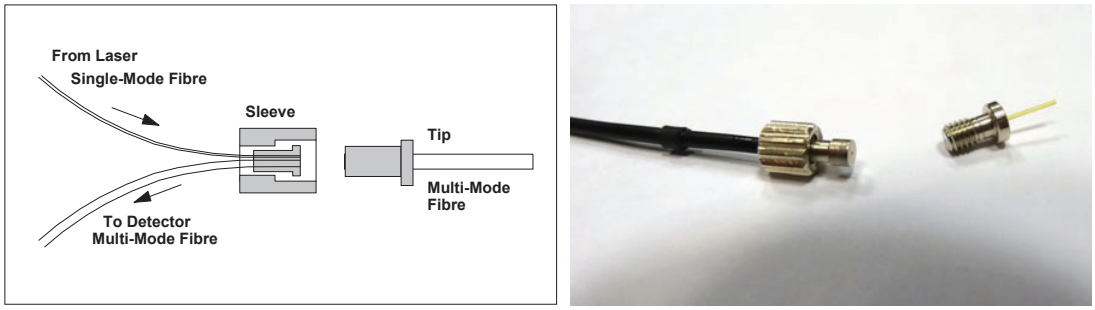

Fig. 776: Fibre probe with a removable tip

Tissue Scanning System with Laser Wavelength Multiplexing

Most TCSPC DOT data are under-sampled in space and in wavelength: The optical signals are collected by fibres or fibre bundles at a moderate number of spatial positions, and a few lasers (usually two) of different wavelength are multiplexed. Undersampling poses a significant problem to spatial reconstruction. For small-animal imaging the problem has been partially solved by moving the detector setup and the subject, see Fig. 781 and Fig. 782.

A setup for scanning stationary objects in space and wavelength has been built and tested in cooperation of bh and the Physikalische Bundesanstalt Berlin (PTB). We thank Michail Mazurenka and Heidrun Wabnitz for their cooperation. The principle is in Fig. 777.

The measurement object is scanned by a laser beam via a fast galvanometer scanner. The scanner is driven by a bh GVD-120 scan controller the same way as in the bh confocal FLIM systems [63]. The light returning from the sample (diffuse scattering or fluorescence) is separated from the excitation beam by a beam splitter. The light passes a filter and a pinhole, and is detected by an HPM-100-50 hybrid detector. The single-photon pulses from the detector are recorded by an SPC-150 TCSPC FLIM module. The pixel, line, and frame clock pulses for synchronisation with the scan are delivered by the GVD-120 scan controller.

A supercontinuum laser delivers the pulsed excitation light. We used a Fianium SC400 laser (40 MHz version) with an AOTF-V1-HP tuneable acousto-optical filter (AOTF). The AOTF is able to select between eight programmable wavelengths by signals applied to the 'MOD' inputs of the AOTF controller. These signals are provided by a counter that is driven by the frame clock pulses of the scan controller. The result is that the AOTF cycles through the 8 wavelengths for subsequent frames of the scans. Simultaneously, the routing inputs of the SPC-150 module are driven by signals from the counter outputs. Thus, the SPC module builds up separate images for the individual laser wavelengths.

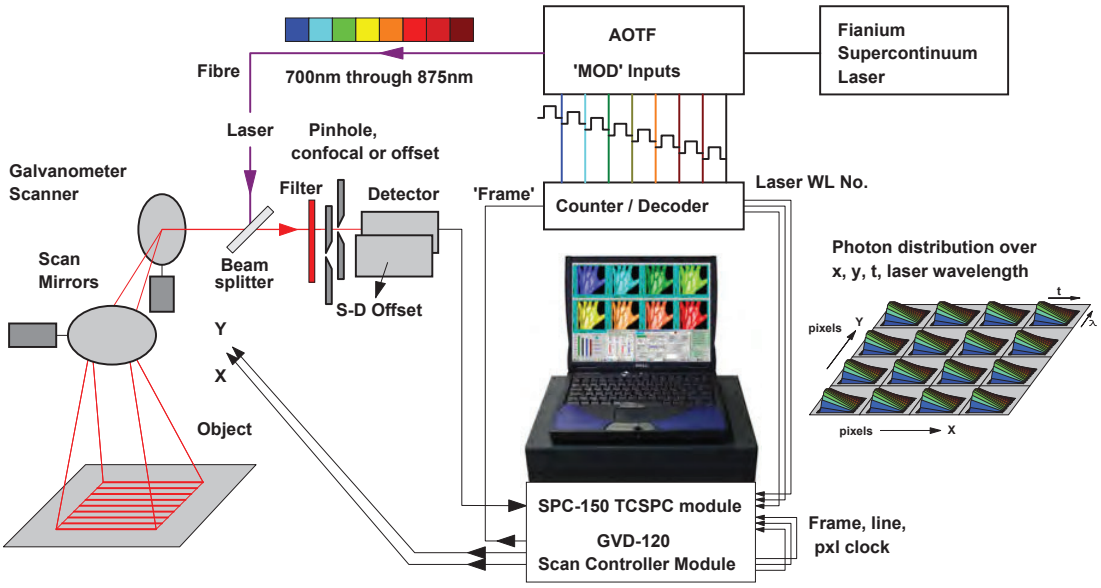

Fig. 777: Scanning system with wavelength multiplexing

The detector and the pinhole can either be made confocal with the laser spot in the sample plane, or offset by a few millimeters. A filter in front of the detector selects either diffusely scattered light or fluorescence. A typical result is shown in Fig. 778.

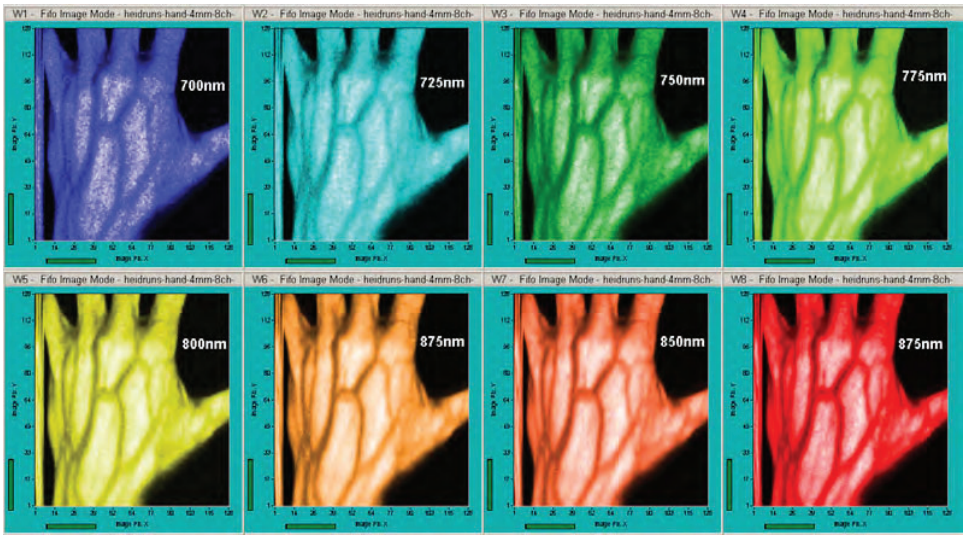

Fig. 778: Diffuse-reflection scan of a human hand. Source-detector offset 4 mm, wavelengths indicated in the images. False colour, selected to indicate the different laser wavelength.

Fig. 779 shows two images analysed by bh SPCImage FLIM analysis software. Both are from the 820-nm channel, and show the first moment, M1, coded in colour. The left image is for a source-detector distance of d = 0 mm, the right one for a distance of d = 4 mm. Both images show differences in M1 between the blood vessels and the surrounding tissue. As expected, the difference depends on the source-detector distance: For d = 0 it is only 3.5 ps, whereas it is almost 22 ps for d = 4 mm.

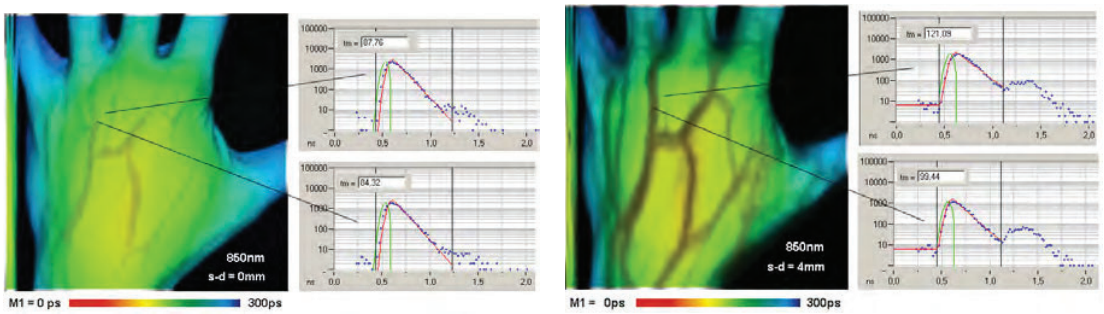

Fig. 779: M1 images of the data in the 820-nm channel. d = 0 (left) and d = 4 mm (right). Analysis by bh SPCImage FLIM analysis software.

Fig. 779 shows also two problems of the setup. The first one is that the measurement object is not flat. Consequently, there are path length differences that show up in the M1 data. This problem can be solved by taking a reference scan at d = 0 and using it as a reference for scans at larger distances. The path-length can also be eliminated by using the second moment, M2. Another problem is reflection and scattering in the optical setup. The laser is scattered and reflected at any optical surface in the beam path. Because excitation and detection use the same beam path reflections show up in the time-resolved data, see bumps at late times in the DTOFs shown in Fig. 779. The reflections can only be minimised by carefully selecting the optical components, by using anti-reflection coatings, and by avoiding optical surfaces in planes conjugate with the pinholes.

Another way to mitigate the influence of optical reflections is to use a time-gated SAPD (see Gated SPADs, page 180) as a detector. To explore the options of time-gated detection a single-point (non-scanning) setup was built up and evaluated [764]. This setup was then upgraded with scanning and multiplexing of two wavelengths [765] by the principles shown in

Fig. 777. Results were presented in [765] and [1194]. A characterisation of the system has been given in [348].

Optical reflections are not a problem when the scanner is used to detect fluorescence. They are then suppressed by the fluorescence filter. An example of fluorescence recording is shown in Fig. 780. Interestingly, the ICG lifetime is not constant, see also FLIM images in Fig. 534, page 369.

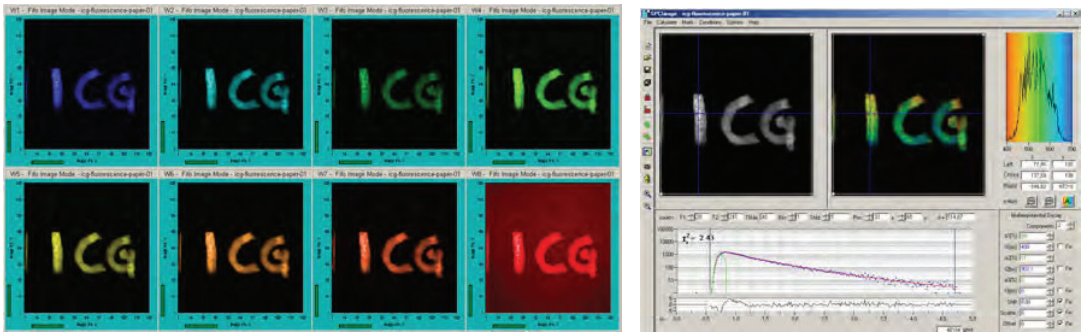

Fig. 780: Left: Fluorescence images of ICG on paper. Excitation wavelengths from 701 nm (upper left) to 780 nm (lower right). Fluorescence was detected from 800 nm to 850 nm. Right: Lifetime analysis with SPCImage, excitation channel 770 nm.

Muscle and Bone Studies

Time-resolved DOT is sometimes used for optical biopsy of bone tissue, and to track heamodynamics and oxygen kinetics in muscle tissue. Compared with instruments used for structural brain imaging the number of source and detection channels is normally considerably reduced.

Instruments described in [302, 305, 1147] used two lasers multiplexed pulse-by-pulse and eight detection channels routed into a single SPC-630 channel. An instrument described in [48] used super-continuum generation in a photonic crystal fibre and a multi-wavelength TCSPC system based on a PML-16 and an SPC-630. Absorption and scattering coefficients were obtained at 16 wavelengths simultaneously. Binzoni et al. describe an instrument based on an SPC-130, a supercontinuum laser, and wavelength multiplexing by a rotating filter wheel. The instrument was used for characterisation of bone tissue phantoms [180].

An instrument for optical biopsy of bones based on a diode laser and a single SPC-330 TCSPC channel was described in [379, 380]. Other instruments use a tuneable synchronously pumped dye laser and a Ti:Sapphire laser [888]. The lasers are switched into a single source fibre by a fibre switch. A single SPC-630 channel records the diffusely reflected light and a reference signal split off from the source fibre.

Fluorescence Lifetime Detection in DOT

The fluorescence lifetime of a fluorophore depends on its local environment. The lifetime of many fluorophores changes upon binding the protein and DNA. Extremely large changes can be obtained from FRET probes that contain a donor and an acceptor at the ends of a protein chain. The lifetime of the donor then depends on the folding of the protein chain. The folding changes upon binding to other proteins, and so does the lifetime of the donor. It is expected that such probes can be constructed to mark specific binding targets.

Fluorescence DOT as a diagnostic tool of human medicine is in an early stage, mainly because potential probes are not approved for the application to human patients. So far, only indocyanine green (ICG) can be used. ICG in water has a fluorescence quantum yield of about 4% [328]. The fluorescence lifetime of ICG bound to human serum albumin (HSA) in water was determined to be double exponential, with contributions of 84% of 615 ps and 16% of 190 ps [438, 745]. Please see also section 'Near-Infrared FLIM' page 367 in this book. The lifetime is clearly dependent on the solvent; for pure ICG in ethanol 550 to 650 ps are obtained, see Fig. 764. Lifetimes this short are difficult to separate from the time-of-flight distribution in thick, inhomogeneous tissue. It is therefore difficult to exploit possible lifetime changes of ICG for tissue characterisation.

Another problem is the extraction of fluorescence lifetimes from DOT data. The extraction of pH-induced fluorescence lifetime variations from time-of-flight curves recorded by TCSPC was studied in [428]. The fluorescence of beads stained with IRD38 (Li-Cor, Inc.) embedded in agarose phantoms was recorded by TCSPC. A femtosecond titanium-sapphire laser was used for excitation, and a H7422-50 PMT module for detection. The decay curves were recorded by an SPC-730 TCSPC module. The authors show that the fluorescence decay can be separated from the instrument response function and the time-of-flight distribution of the bulk medium.

Small-Animal Imaging

Small-animal imaging is not limited by the strict constraints placed on DOT in human patients. Thus a large number of exogenous fluorophores can be used [1026]. Moreover, the typical tissue thickness is only a few millimeters, so that the excitation wavelength is not restricted to the NIR only. Visible and UV excitation can be used to excite not only exogenous, but also a large number of endogenous fluorophores, including NADH, or GFP and its mutants in transgenic organisms. The non-invasive character of DOT allows one to track the growth of a tumor, angiogenesis, invasion and metastasis, the progress of photodynamic therapy, or the effect of drugs [304, 1026].

A complete time-resolved small-animal imager was available from ART Advanced Research Technologies Inc., Montreal, Canada. The animal (a mouse or a rat) was placed on a platform mounted on a translation stage. Scanning in the X direction was accomplished by moving the translation stage. In the Y direction the laser beam is scanned by a galvanometer mirror. The fluorescence light was collected by a lens, descanned by a second galvanometer mirror, and detected by a PMT. The signal was recorded by an SPC-130 TCSPC module. First results were presented by Gallant et al. [425]. Detection of a tumor in a mouse was demonstrated in [199]. A dye-labelled hexapeptide was used as a tumor marker. The marker accumulated in the tumor and the major excretion organs. In the tumor a fluorescence lifetime of 1.03 ns was found, compared to 800 ps in other tissue. Unfortunately, ART went out of business, and this wonderful instrument disappeared from the market.

A system that records steady-state fluorescence images and time-resolved fluorescence data in single points by an SPC-130 card was described in [1166]. The authors used the instrument to observe the effect of vascular disruption agents on tumors in mice.

A scanning system that records the images of the time-resolved fluorescence, diffuse fluorescence, diffuse transmittance, and fluorescence from both sides of a sample was described in [211]. The data in the four channels were recorded by an SPC-134 TCSPC system. The instrument was demonstrated on phantoms containing a fluorescent inclusion.

An instrument developed by Gao et al. uses the four parallel TCSPC channels of an SPC-134 and multiplexes four signals into the detector of each channel by 4:1 fibre switches [432, 738]. The laser was multiplexed into several source positions by another fibre switch. The instrument was demonstrated on small-animal-sized phantoms but was certainly capable of being used on the animals themselves. Image reconstruction procedures for the recording geometry used were described by Ma et al. [738] and Yang et al. [1245].

A small-animal system of the classic tomographic architecture has been built by Kepshire et al. [597, 598]. The principle of the system is shown in Fig. 781.

The specimen is illuminated by a single laser beam. A gantry with five collection lenses is rotated around the specimen. The collected light is projected into optical fibres which transfer the light to the detectors. The light of each channel is split into a transmission and a fluorescence component. Both components of each channel are detected by H7422P-50 PMT modules. The PMT pulses are fed into three routers and processed by three TCSPC channels of the SPC-134 package. The forth TCSPC channel records a reference pulse from the laser. The signal is used to eliminate intensity variations and temporal drift.

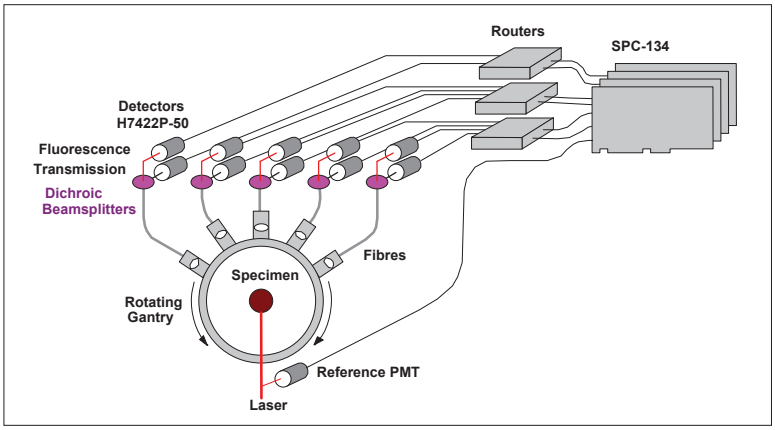

Fig. 781: Small-animal fluorescence tomography system used by Kepshire et al.

The system was used for tomographic imaging of a glioma tumor in a mouse. The authors exploited the fact that glioma tumors have increased concentration of protoporphyrin IX (PpIX). The concentration was further enhanced by administration of aminolevulinic acid (ALA). PpIX was excited at 635 nm and detected from 650 nm to 700 nm. The setup was sensitive enough to detect a clear signal form the PpIX. The tumor image was reconstructed from the ratio of the fluorescence and transmission intensities. Because fluorescence and transmission data are acquired simultaneously this ratio is resistant to most calibration errors, distance changes, and tissue inhomogeneities. The data obtained this way were combined with micro CT data obtained from the same animal. Please see [597, 598] for details.

Another non-contact tomographic system with 7 fluorescence channels and 7 reflection channels has been built by Lapointe, Pichette, and Berube-Lauziere [677]. The basic optical architecture is shown in Fig. 782, left. The subject is placed on a shaft that can be rotated and shifted vertically. Fluorescence is excited by the beam of a Ti:Sapphire laser. Each optical detection channel contains a lens system that projects a small area of the subject on two PMC-100-20 detectors. One detector is used for fluorescence, the other for reflection. A dichroic beamsplitter in the beam path splits the light into a the two channels; filters are blocking unwanted spectral signal components. Adjustable irises in front of the detectors are used for regulation of the active detection area. The photon pulses from all 14 detectors are routed into the four TCSPC channels of an SPC-134 package.

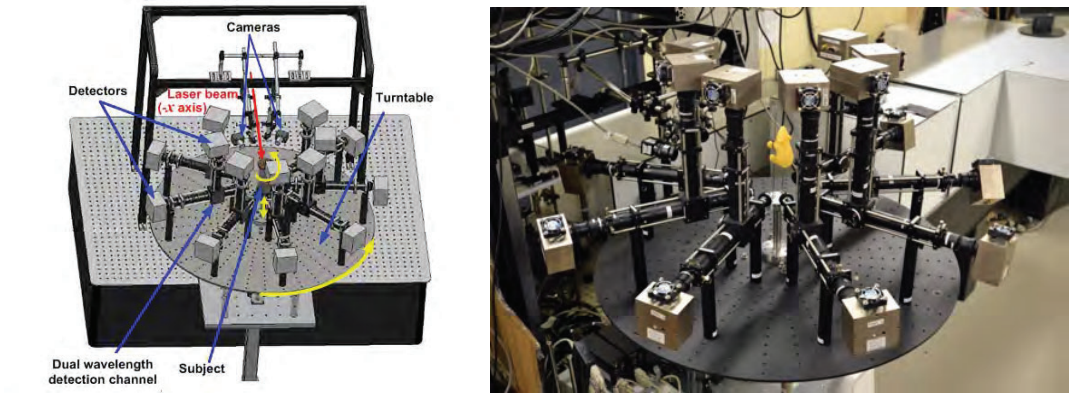

Fig. 782: Fluorescence tomography setup of Lapointe, Pichette, and Berube-Lauziere. 7 detection channels containing a fluorescence and a reflection detector each can be rotated around the sample.

Mu, Pera and Niedre built a dual-channel multi-wavelength fluorescence and diffuse reflection imaging setup [817]. It consists of a supercontinuum laser, two nested motorized rotation stages, two PML-16-C multichannel detectors, and two SPC-130 TCSPC modules. The rotation stages move both the sample and the detector positions so that tomographic imaging under different projection angles is performed. From the laser, two illumination beams are derived. The first one is used for fluorescence imaging, and has a spectrum from 630 to 680 nm. The second one is used for diffuse reflection imaging, and has a spectrum from 550 to 850 nm. The principle is shown in Fig. 783, left, a photo of the setup is shown in Fig. 783, right.

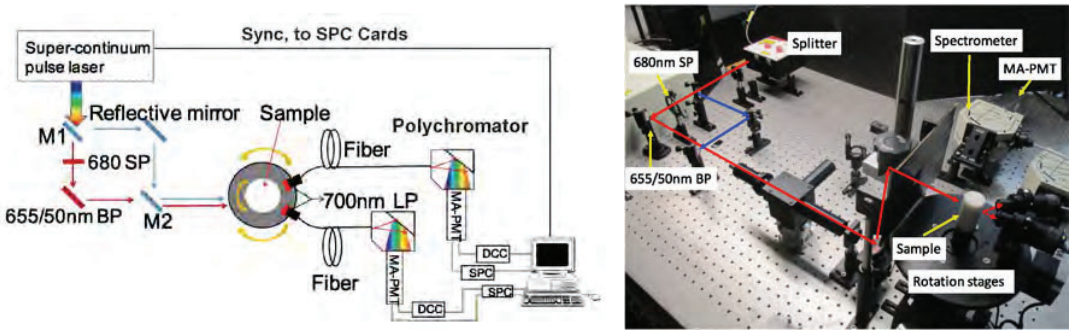

Fig. 783: Multi-wavelength fluorescence and diffuse reflection imaging setup of Mu, Pera and Niedre. Adapted from [817].

The authors verified the instrument and the data analysis algorithms with phantoms, and demonstrated that they obtain homographic images for four fluorophores with 1 mm or better spatial resolution. An similar setup with two SPAD detectors instead of the 16-channel PMTs is described in [816].

Technical Issues of DOT

Pulse Dispersion in Optical Fibres

Almost all devices for diffuse optical tomography are using fibres or fibre bundles to transmit the light from the lasers to the patient and to feed the diffusely transmitted or reflected light from the patient into the detectors. The fibres do not only simplify the optical setup but also decouple the patient electrically from the recording electronics. Unfortunately the temporal dispersion in the fibres noticeably impairs the time resolution. Moreover, the effective instru-

ment response function (IRF) depends on the numerical aperture of the light cone coupled into the fibres. The effective aperture can be different for the recording of the IRF and the time-of-flight distribution at the patient, and severe errors in the determined optical properties can result [716]. A solution to the dispersion problem is to use a thin diffuser for IRF recording. The diffuser is placed in front of the detector fibres and illuminates the fibre with the same aperture as the sample. Because a thin diffuser does not broaden the IRF noticeably the recorded IRF shape has been found very close to the correct one [716].

Any other optical elements that can change the effective numerical aperture at the entrance or exit if a fibre or fibre bundle have to be strictly avoided. Under no circumstances an iris should be used for intensity regulation. However, also absorptive and reflective neutral density filters yield different attenuation for rays of different obliquity.

Changes of the effective NA can be particularly strong if a narrow-band interference filter is placed in the light cone in front of the fibre. The transmission wavelength of an interference filter shifts to shorter wavelength for oblique rays. With a narrow-band filter in a divergent or convergent beam, the outer part of the useful NA of the fibre can be entirely blocked by the filter. The correct solution is to put the filters into a collimated part of the beam.

Collimation of the filter beam path is important also for fluorescence detection in a DOT setup. To separate the fluorescence from the much stronger excitation light, an extremely steep long-pass interference filter has to be used. If this filter is not used in a parallel beam, the filter transition broadens towards shorter wavelengths, with disastrous effect on the blocking of the excitation light.

Laser Multiplexing

Most of the currently existing DOT systems multiplex lasers pulse-by-pulse. This technique has a number of serious drawbacks: It reduces the effective stop rate of the TCSPC modules by the number of laser. This increases possible pile-up effects. Moreover, pile-up and counting loss in the signal of one laser influences all signals later in the multiplexing period. The result is intensity crosstalk between the laser channels. There is also crosstalk by optical reflections on the fibres. A reflection from one laser channel normally shows up in the time interval of another channel. The result is warp in the waveform recorded in this channel dependent on the signal size of the channel that causes the reflection. Finally, thee is also crosstalk due to detector afterpulsing. The afterpulsing background is proportional to the total signal. However, the afterpulsing background of the detector is recorded in all laser channels. Consequently, there is also a crosstalk in the background. The effects are shown graphically in section ‘Multiplexing of Lasers’, page 287.

A better way to record signals excited by several laser is to use the multiplexing capability of multi-dimensional TCSPC, see ‘Multiplexed TCSPC’, page 102 or ‘Multiplexing of Lasers’, page 287. The lasers are multiplexed in microsecond or millisecond intervals, and the routing signals are used to send the photons into separate memory blocks. The stop rate is the full laser repetition rate, and the TAC range needs not to be no longer than the signal duration. Pile-up, counting loss, reflections, and afterpulsing in one channel does not influence other channels. Another advantage is that that multiplexing on the microsecond or millisecond time scale can be used with the AOTFs of supercontinuum lasers, as shown in Fig. 777, page 570.

Detectors

Time Resolution

The typical width of the time-of-flight distributions recorded in DOT is on the order of a few ns. Therefore a detector IRF width of 150 to 300 ps is normally sufficient. Even longer detector IRFs are sometimes tolerated, especially if the pulse dispersion in long fibre bundles dominates the IRF width. It can, however, be expected that the stability of a curve fitting procedure and the standard deviation of the first and second moments of the recorded signal shape decrease dramatically when the IRF width reaches or exceeds the true width of the time-of-flight distribution.

More important than the IRF width is the IRF stability. To reveal effects of brain activity, variations corresponding to changes in the first moment (M1) of a few ps must be reliably recorded. Maintaining a timing stability of a few ps over a wide range of count rates is anything but simple. The most critical parts of the system are the PMT and its voltage divider.

Extremely good timing stability has been obtained with the H5773, H5783 photosensor modules and, consequently, with the bh PMC-100 detectors that are based on these modules (see Fig. 242, page 156). Also the H7422 modules yields good timing stability [140].

Background

Detector background has a detrimental effect on any time-resolved optical measurement. As an example, Fig. 784 shows a distribution of time-of-flight (DTOF) recorded with 1 % background. The influence of the background does not look dramatic, and one might presume that the effect can be ignored.

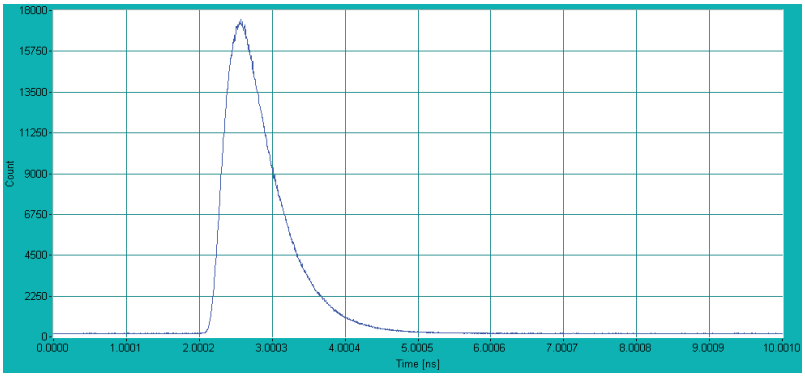

Fig. 784: DTOF recording with a background of 1% of the peak intensity

Now consider what happens when the first moment of the DTOF is calculated: The FWHM of the DTOF is 0.7 ns, and it contains approximately $3{\cdot}10^6$ photons. The FWHM of the background is 10 ns. There are approximately 425,000 photons in the background.

When the first moment is calculated the arrival times are added and divided by the number of photons. The absolute noise of the sum of the arrival times for the photons in the DTOF and in the background is about $FWHM\sqrt{N}$. One might presume that the background does not add much noise because it contains far less photons than the DTOF. However, the FWHM of the background is 10 ns, whereas the FWHM of the DTOF is only 0.7 ns. The absolute noise contributions are thus

$0.7ns\sqrt{3{\cdot}10^6}$ = 1212 ns for the DTOF photons and

$10ns\sqrt{425000}$ = 1955 ns for the background photons

In other words, the timing noise contribution from the background is larger than the noise induced by the statistics of the DTOF photons!

Subtraction of the background does not help because it does not reduce the contribution of the timing noise to M1. Keeping the recording (or calculation) time interval as small as possible may help a bit, but the only efficient way to obtain near-ideal signal-to-noise ratio of M1 is to reduce the frequency of background counts.

Unfortunately, attempts to reduce the background by cooling the detectors are only partially successful: Most of the background in PMTs and SPADs comes from afterpulsing. The reason of afterpulsing in PMTs is ionisation of rest gas molecules, in SPADs it is trapping and diffusion of electrons and holes of the previous avalanche breakdown. Although afterpulsing can be slightly reduced by optimising the detector operating voltages a dramatic improvement is only possibly by special detector design.

The only large-area detector free of afterpulsing background known so far is the hybrid PMT. Fig. 785 shows a DTOF recording by a HPM-100-50 hybrid detector module (left) and by a R7400 PMT (right). The better dynamic range of the HPM recording is due to the absence of afterpulsing.

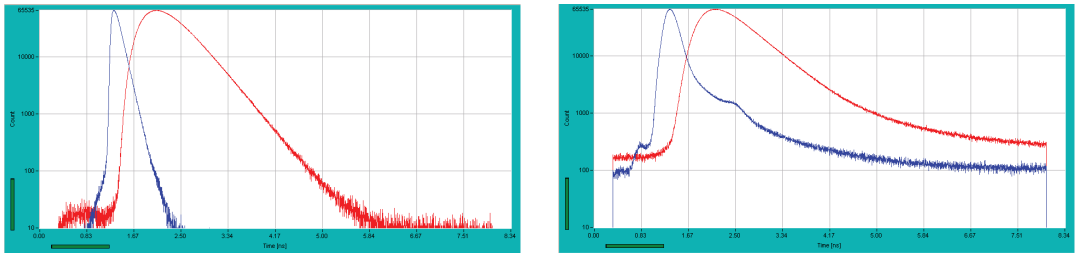

Fig. 785: DTOF recorded with a bh HPM-100-50 hybrid detector module (left) and with an R7400 PMT (right). The DTOF is shown red, the IRF blue.

Efficiency

TCSPC-based DOT requires PMTs with a high efficiency in the NIR. Although the commonly used multi-alkali cathode works up to 820 nm, the efficiency above 750 nm is not satisfactory. Reasonable sensitivity above 750 nm can be obtained from ‘extended-red’ multi-alkali cathodes. PMTs with these cathodes work up to 850 nm.

Recently, Hamamatsu has developed a ‘high efficiency extended red’ cathode, the NIR efficiency of which comes close to that of the GaAs cathode. The new cathode is available in the H5773-20 and H5783-20 photosensor modules. The high timing stability, the short IRF, and the relatively low price of these modules make them the most useful single channel DOT detectors currently available. However, reasonably low dark count rates can be obtained from these detectors only when they are cooled. Therefore, the bh PMC-100-20 detector module contains a thermoelectric cooler attached to an H5773-20 photosensor module.

The most efficient cathodes in the wavelength range of DOT are GaAs cathodes. Although the cathode efficiency of different devices may differ considerably, a factor of 10 can be gained at 800 nm compared to a conventional multi-alkali cathode. The GaAs PMT module most frequently used in DOT is the H7422-50 [496].

The best DOT detector currently available is the bh HPM-100-50 hybrid detector module. It is based on the new Hamamatsu H10467-50. The detector has a GaAs cathode. Although direct comparisons have not been made yet the efficiency of the HPM-100-50 can be expected even a bit higher than for the H7422-50. Please see ‘HPM-100 Hybrid Detector’, page 161.

Detector Area

In DOT experiments the light is diffusely emitted from a large area of the sample. Whatever optics are used, the intensity per area unit cannot be made higher than at the surface of the sample. That means good sensitivity can only be obtained with a detector of large active area. This is no problem for PMTs which have active areas of at least a few millimeters in diameter.

Active area is, however, a problem to SPADs. Fast SPADs have diameters of 50 to 100 µm [551, 785]. Compared with a PMT of 5 mm diameter the area is 2500 to 10,000 times smaller and so is the detected signal. Although SPADs have good quantum efficiencies in the NIR they cannot compete with PMTs in terms of sensitivity.

Fig. 786 shows a comparison of an MPD PDM-50 SPAD with a HPM-100-50 hybrid detector module. The SPAD has an active diameter of 50 µm, the hybrid detector of 3 mm. The quantum efficiencies are approximately the same.

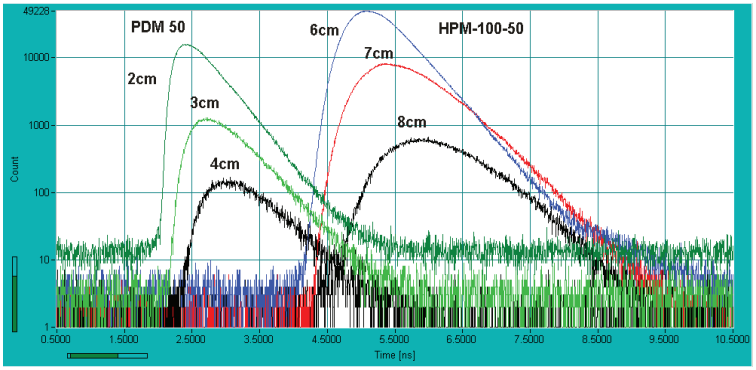

Fig. 786: Comparison of a 50µm SPAD with a hybrid PMT of 3mm active diameter. Phantom measurement, numbers indicate source-detector distance

The comparison was done at a phantom with realistic optical properties. With the SPAD, reasonable signals were obtained for source-detector distances of 2, 3 and 4 cm. With the hybrid detector good signals were obtained for 6, 7, and 8 cm. Shorter distances were not used because the signals caused overload in the detector. (Of course, signals at shorter distance can be recorded with ND filters.) The results are interesting in several respects.

First, the results confirm a general rule of thumb of optical tomography: The intensity drops by about an order of magnitude for every centimetre increase in source-detector distance.

Second, from the results it can be estimated that the HPM-100-50 detects about 10,000 times more photons than the SPAD.

Third, this huge increase in sensitivity translates into an increase of the applicable source-detector distance by a only factor of two. A factor of two may be a lot when penetration depth into tissue is considered but it is ridiculous considering a sensitivity ratio of four orders of magnitude. This should be kept in mind when different detectors are compared: Sensitivity differences have minuscule influence on the maximum source-detector distance unless they are larger than an order of magnitude. Even the SPADs with their tiny area deliver good results if the source-detector distance in no larger than 4 cm.

The dependence of the intensity on the source-detector distance should be kept in mind also when laser power is considered. Compensating for intensity drop at increased source-detector distance by increased laser power soon leads to unrealistic power levels.

Download publications at https://www.boselec.com/resource/
or email or mail this form to us.

Boston Electronics

91 Boylston Street, Brookline, MA 02445
tel: (617)566-3821 www.boselec.com
tcspc@boselec.com

Request a *FREE* bound copy of:

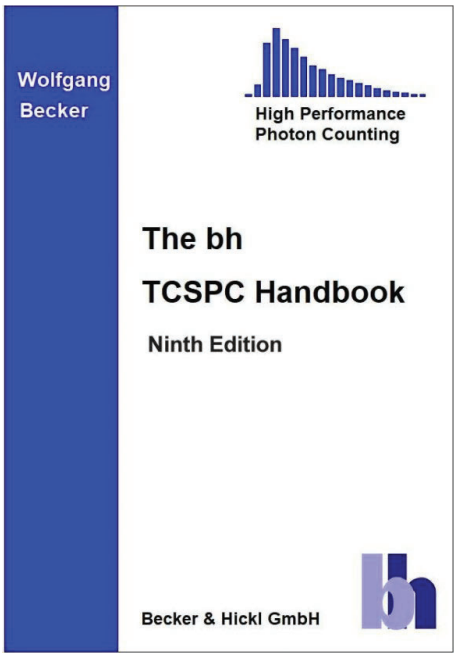

The Becker & Hickl TCSPC Handbook

9th Edition, 900+ pages, 1283 References, October 2021 by Wolfgang Becker

For your copy, tell us something about your interest in TCSPC and give us your name and address below so that we can send it to you.

❒ I am a TCSPC user now
❒ I am thinking about using TCSPC in the future
❒ My interest is microscopy
❒ My interest is single molecule detection
❒ My interest is _____

Name: _____

Company or Institution: _____

Address: _____

Also available useful publications (check the box to request):

❒ TCSPC for Microscopy
❒ TCSPC Systems
❒ Photon Counting Detectors for TCSPC
❒ Picosecond Lasers for TCSPC
❒ Becker & Hickl Catalog

ALL PUPLICATIONS ARE AVAILABLE FOR DOWNLOAD AT
https://www.boselec.com/resource/

12/31/2021